To boldly go into the next dimension: 3D raypath interferometry issues

David C. Henley

ABSTRACT

The technique known as raypath interferometry was developed to correct seismic reflection data for difficult near-surface conditions by generalizing and relaxing the assumptions used by conventional surface-correction algorithms (residual statics). We have demonstrated the success of the technique on model data as well as on several sets of 2D field data, both PP and PS. The method improves not only the alignment and coherence of reflection events, but also their waveform consistency.

We have begun to extend raypath interferometry to 3D. In previous work, we introduced the source-receiver azimuth as a third dimension for grouping 3D traces for analysis. Using common-azimuth bins, we need only a 2D trace transform (initially the RT, or radial trace transform) to move the 3D data to a common-raypath domain for applying interferometry. We demonstrated the success of this approach by applying it to the vertical component of the Blackfoot 3D-3C field data, and showing improved event coherence at all stages of the process except the CMP stack, which was not computed due to limitations in our inverse RT Transform.

Here, we apply raypath interferometry to the radial horizontal (PS) component of the same Blackfoot data set. As with the PP component, we demonstrate improved event coherence, but do not compute CCP stack traces, due, once again to our limited RT Transform preventing a proper inversion. Hence, we explored the alternative of replacing our RT Transform with an invertible Tau-P Transform. The Tau-P Transform, however, is not compact, requiring at least an order of magnitude more storage than its input X-T gather, when performed with sufficient resolution to allow high-fidelity inversion.

In future work, we will implement data storage strategies that will enable full comparisons of CMP and CCP stack traces of corrected and uncorrected 3D-3C data.

INTRODUCTION

Correcting land seismic reflection data for the effects of an irregular surface layer is a persistent problem in seismic data processing, and the problem is more difficult for shear-wave or converted-wave data. Fortunately, much seismic data can be corrected by the straightforward process of computing and applying time shifts to align reflection events on the individual traces before stacking them over common CMP or CCP. This process, known as residual statics correction, relies on the following assumptions: the near-surface layer is much lower in velocity than underlying layers, leading to the approximation of 'surface consistency'; and reflected (or converted) events arriving at the surface consist of a single arrival—no accompanying scattered or multi-path events. Henley (2012a) showed how surface consistency could be generalized to 'raypath consistency', of which surface consistency is a special case; and he further showed how raypath consistency implies nonstationary 'statics', or time shifts which vary with transit time. Henley

(2012a) also introduced the concept of surface effect removal by deconvolution of 'surface functions' from seismic traces rather than time-shifting the traces. Surface functions characterize not only the 'direct' arrival from a reflection, but also any multiples, scattered events, or multi-path events associated with the surface layer at specific locations. Furthermore, surface functions can also capture the statistical time uncertainty of the event arrivals; hence the deconvolution of surface functions attempts to remove these effects from the corresponding seismic traces, leaving a consistent event arrival time and waveform from trace to trace. The detection and removal of surface functions by cross-correlation and deconvolution and the adoption of raypath consistency are the two basic concepts which constitute raypath interferometry. The technique was first successfully applied to a set of 2D data from the Canadian Arctic in which surface-consistency and the single-arrival event assumption were both demonstrably violated (Henley, 2006, 2012a), then further demonstrated by application to other, more conventional data sets, including converted wave or PS data (Henley, 2012a, 2012b, 2014).

Nonstationarity

As has been convincingly shown by Cova et al (2013a, 2013b, 2014a, 2014b), most PS data violate the surface-consistent assumption for the shear-wave leg of the converted-wave travel path. They thus require nonstationary (time-varying) corrections, which makes a raypath-consistent approach the most appropriate processing strategy for surface correction, regardless of whether interferometry is used as the mechanism to actually find and apply corrections.

The common-raypath domain

The earliest implementation of raypath interferometry used the radial trace (RT) transform (Claerbout, 1975, 1983) to remap the X-T domain seismic traces to a raypath-dependent domain for computing and applying corrections. The reason for this transform choice is that the RT transform is exactly invertible under certain easily-controlled conditions, with no loss in data fidelity during a forward-and-inverse transform operation. A refinement of the RT transform, known as the Snell Transform (Ottolini, 1981) has been shown to improve the performance of raypath interferometry significantly, if an approximate NMO velocity function is known (Henley, 2014). Cova et al (2014b, 2015) have determined, however, that the Tau-P Transform is also an acceptable pathway to the raypath-dependent domain, as long as the aperture for the transform is large enough to preserve most of the fidelity of the original data. The inverse transform never recovers the original data exactly, but the aperture can be made large enough in most cases to preserve the visible fidelity of the data for one cycle of forward and inverse transform. The Tau-P transform has two further advantages: nothing need be known about the NMO velocities of events; and a commercial Tau-P transform and its inverse preserve the original trace headers of the X-T input trace ensemble and replace them exactly in the inverse transform, using processing package database utilities. Our CREWES-developed RT transform, however, does not, but only interpolates key headers linearly and forces the other headers to constant values, during transform inversion (Henley, 1999). This approach works well enough with 2D data having a reasonably linear surface layout and

nearly regular surface station spacing, but begins to fail with irregular distributions of source-receiver offset values, as we show later.

The interferometry mechanism

There are many different applications of 'interferometry' described in the geophysical literature; but what they all have in common is cross-correlation of raw data traces either with each other or with summed raw traces, and the subsequent use of the cross-correlation functions to correct the raw data. Most applications, like the virtual source method (Bakulin and Calvert, 2006), use the summation of cross-correlations of one raw trace with a gather of similar traces to derive a Green's Function for the common trace, which can then be used to correct this trace to a datum. Our approach, however, uses the cross-correlation of a raw trace with the summation of raw traces within an aperture to estimate a 'surface function', which is then deconvolved from the original raw trace to correct the trace for the irregularity of its particular source or receiver surface point relative to the summed traces (Henley and Daley, 2007). This type of interferometry is most similar to the optical interferometry experiment that most of us encounter in a physics lab, and which is illustrated in Figure 1. In this circumstance, a plane wave impinges simultaneously on a uniform medium and an irregular one. The resulting wavefields are cross-correlated to extract timing and phase differences which constitute the information required to correct the distorted wavefield for the effects of its transmission through the irregular medium.

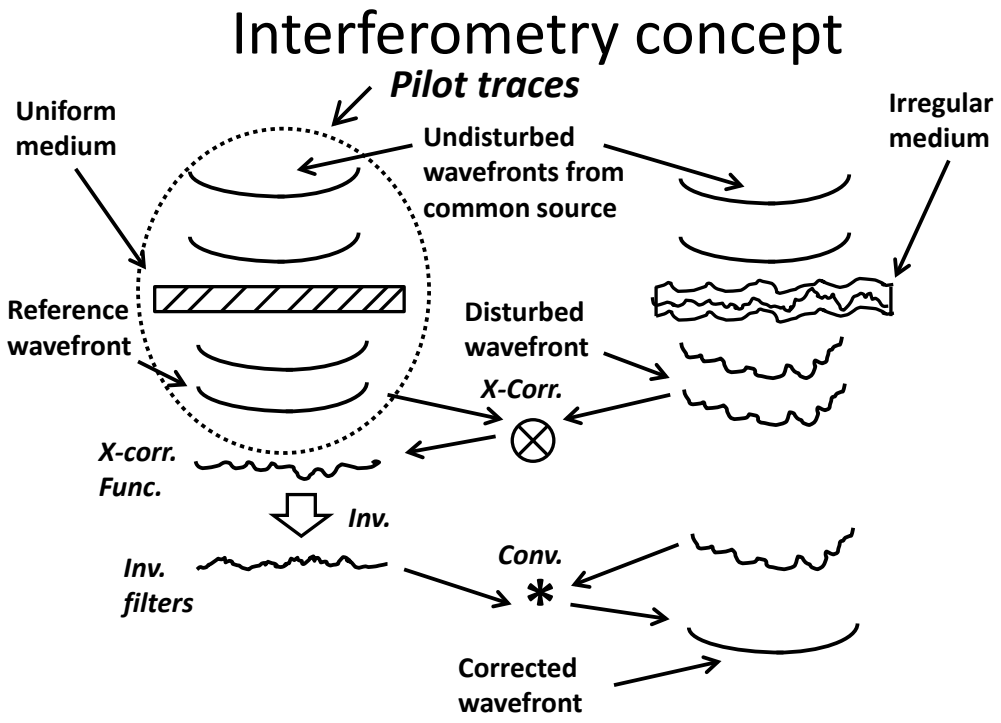

FIG. 1. Schematic illustrating the concept of optical interferometry as applied in raypath interferometry. The key step in this construction is obtaining the reference wavefront (also known as 'pilot traces')

Most conventional autostatics programs rely on cross-correlations between pairs of raw traces, or between raw traces and 'pilot' traces (usually summed raw traces), but they use only the picked delay times of the largest correlation peaks to compute 'statics' or time shifts to apply to the seismic traces whose cross-correlations were used in the computations. Various reconciliation and threshold algorithms are used to reduce the inevitable disparity between correlation peak times used to calculate the statics; and often, these result in a significant portion of raw correlation information being discarded. Finally, autostatics programs rely almost universally on the surface-consistency assumption to compute statics values.

In the interferometry approach, however, each cross-correlation function is used in its entirety to deconvolve its corresponding trace, which results not only in a net time shift of the trace, but also correction of phase disparity between the raw trace and its corresponding pilot trace. Furthermore, interferometry can be configured and applied not only to data where surface consistency holds, but to data where only the more general principal of raypath consistency applies, and where nonstationarity must be accommodated.

Raypath interferometry

When we combine the two concepts outlined in the preceding sections--doing surface corrections in some 'common-raypath' domain, and using cross-correlation and deconvolution to find and apply the corrections--we form the technique which we call 'raypath interferometry. We have demonstrated the success of the method on several examples of field data (Henley, 2006, 2012a, 2012b, Cova et al, 2013a, 2013b, 2014a, 2014b, 2015), not only vertical component (PP) data, but also on horizontal component (PS) data. We have also identified what we feel are the key issues involved in its application, particularly those relating to the forward/inverse transform to the chosen common-raypath domain, and to the computation of the 'reference wavefield', or pilot traces.

Transform limitations—RT Transform

While the radial trace (RT) transform is an exact mapping, in order to preserve input data fidelity, the number of traces in the RT domain is almost always much larger than that in the original X-T domain. This creates the problem of retaining the trace headers from each original X-T input gather for placement in the X-T gather created by RT inversion. When we originally programmed our RT forward/inverse algorithm, we chose to store only a handful of X-T trace header values in the newly created RT trace header array (Henley, 1999), most importantly source-receiver offset and CMP. What we actually retained was the min and max offset values, and the min CMP and CMP increment. From these values, stored in unused headers of *each* RT trace, we could then approximately re-create, by linear interpolation, the full range of offset and CMP values in the X-T traces output from the RT inverse transform. Most importantly, we could sort RT trace gathers into different trace arrangements and back while retaining enough information with *each* RT trace to help approximately re-create the original X-T gathers. This scheme works well enough for typical 2D data, since source/receiver gathers tend to be uniformly sampled in both offset and CMP. We encounter difficulties, however, as soon as we encounter trace gathers where source positions are not collinear with receiver

arrays, as in the receiver line gathers of typical land 3D source gathers. Since the offset distribution in each receiver line gather (except the one containing the source point) is non-linear (Henley, 1999, 2015), using our forward/inverse RT transform will result in inaccuracies proportional to the deviation of the offset distribution from linearity. This issue first became obvious when we began the extension of raypath interferometry from 2D to 3D (Henley, 2015), and it prevents the completion of the raypath interferometry process on 3D data using the existing RT transform.

Transform limitations—Tau-P Transform

The Tau-P transform, on the other hand, is *not* perfectly invertible, since it is a discrete approximation of the Radon Transform, with a *limited aperture*. The continuous Radon Transform has an exact inverse because the forward process provides an infinite set of 'projections', at all possible angles, of the input data array. This set of projections can then be 'back-projected', at all angles, to perfectly recover the original data. Reducing the set of projections to a uniformly distributed finite subset at uniform angular increments reduces the fidelity of the inversion only slightly; but removing large angular sectors of the projections (thus limiting the aperture) can affect the lateral resolution quite dramatically. Offsetting these invertibility limitations, however, is the fact that commercially written Tau-P transform packages retrieve the exact original X-T trace headers from the processing package database when the Tau-P transform is inverted. This means that Tau-P transforms can be sorted, processed, and re-sorted to their original order; and that the inverse transform will obtain the original headers during the back-projection process, regardless of the distribution of offsets in the original X-T gathers.

Moving from 2D to 3D

3D surface function

One way to expand raypath interferometry from 2D to 3D is to extend the concept of the surface function, first described by Henley (2012a) from 2 dimensions to 3, then to determine and construct the ensembles of raw 3D traces that most readily allow estimation and removal of these 3D surface functions from the data (Henley, 2015). Figure 2 shows the 1D and 2D surface function schematically, then illustrates the expansion to 3D by introducing a new independent variable, azimuth. In this concept, a 3D surface function is a time series (wavelet) whose shape describes the distribution, timing, and phase of reflection arrivals at a specific surface location, raypath angle, and source-receiver azimuth.

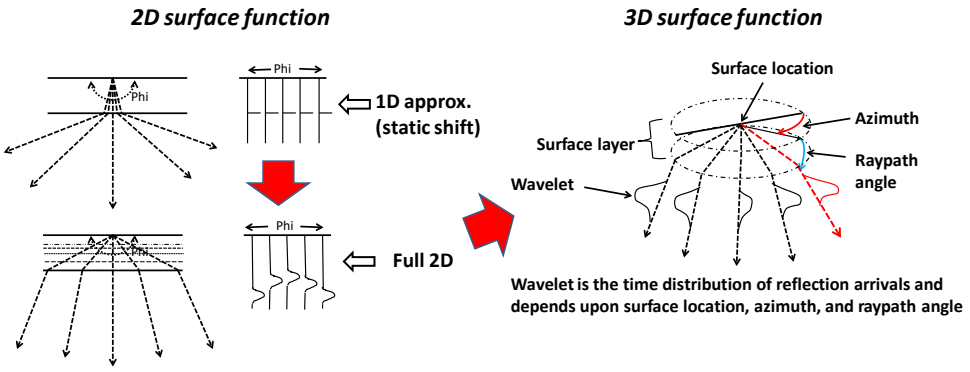

FIG. 2. Schematic showing the extension of 1D surface function (static) to 2D, then full 3D.

Conceivably, a 3D surface function could be constructed using Cartesian coordinates, rather than polar coordinates, such that the amplitude values along any vector extending from the surface location into the subsurface would represent the bulk shift and phase modification experienced by a wavefront perpendicular to the vector. Compared to the polar representation of the surface function described above, however, this seems unnecessarily complicated, particularly since the seismic raypaths would need to be projected onto Cartesian coordinates as well.

Data coordinates

Because our usual mapping coordinate system is Cartesian, the surface stations of all seismic surveys, both 2D and 3D are referenced to Cartesian coordinates. In two dimensions, when we introduce surface functions and common-raypath processing, it is relatively easy to equate raypath direction to the ray parameter of whichever transform we use to convert X-T domain seismic data to the raypath domain, since raypaths are all coplanar with the surface profile of the survey and related by simple plane trigonometry to the coordinates of surface location and travel time. In 3D, however, if we use the ray parameter as direction indicator for raypaths, we must extract 2D planes of data from the 3D survey in such a way that the raypaths in the transformed data are still approximately coplanar. The most natural way to do that appears to be to introduce an additional coordinate into the 3D trace headers—the surface azimuth from source position to receiver position. The new coordinate allows us to sort 3D data into trace ensembles with approximately coplanar raypaths. We can then use a 2D transform to move from the X-T domain to the raypath domain, rather than introduce a formal 3D Radial Trace Transform or 3D Tau-P Transform.

Other dimensional considerations

Most of the additional complexity of performing raypath interferometry in 3D consists of introducing the 3D surface function, then organizing the input data into trace ensembles which lend themselves to 2D transformation into the raypath domain, in coordinate space which is compatible with the 3D coordinates chosen for the surface functions. There is one additional consideration, however; the 3D wavefield being corrected for near-surface effects is a 3D surface, rather than a 2D curve, as in the 2D

case. This means that the 'reference wavefield' must also be a 3D surface. Hence, it is no longer sufficient to perform smoothing along a horizon in one direction to get the reference wavefield—the smoothing must be 2D, as well.

Ideally, we would like to smooth along a horizon in the azimuth plane of a selected trace ensemble, followed by smoothing orthogonal to the azimuth plane. In actual practice, however, this appears to be cumbersome and probably unnecesary; and it appears that smoothing along a secondary, but non-orthogonal parameter direction, while not ideal, is sufficient to create the areally smooth wavefield surface needed for correlating the common-raypath traces in the input ensembles to estimate surface functions (Henley, 2015).

The most troublesome dimensional issue when extending raypath interferometry from 2D to 3D seems to be the difficulty of constructing trace ensembles representing coplanar raypaths that are both evenly sampled and well-populated. Because the original 3D seismic acquisition geometry is Cartesian, imposing the azimuth-oriented ensemble geometry required for gathering coplanar raypaths leads to difficulty in creating a relatively uniform set of ensembles for the entire 3D prospect. Figure 3 illustrates the difficulty of forming ensembles based on angular segments (azimuth bins) from seismic traces acquired using typical 3D source-and-receiver-line land seismic geometry, and Figures 4 through 7 show the distribution of ensembles created with various azimuth bin limits. It is obvious from these figures that for the narrowest bins, the number of traces per ensemble is too small, and there are many bins with too few traces to yield a meaningful raypath transform. For the wider bins, although the raypaths are less constrained to be coplanar (hence making the data less suitable for 2D transforms), the bin populations are much larger, and the trace distributions more nearly linear in offset.

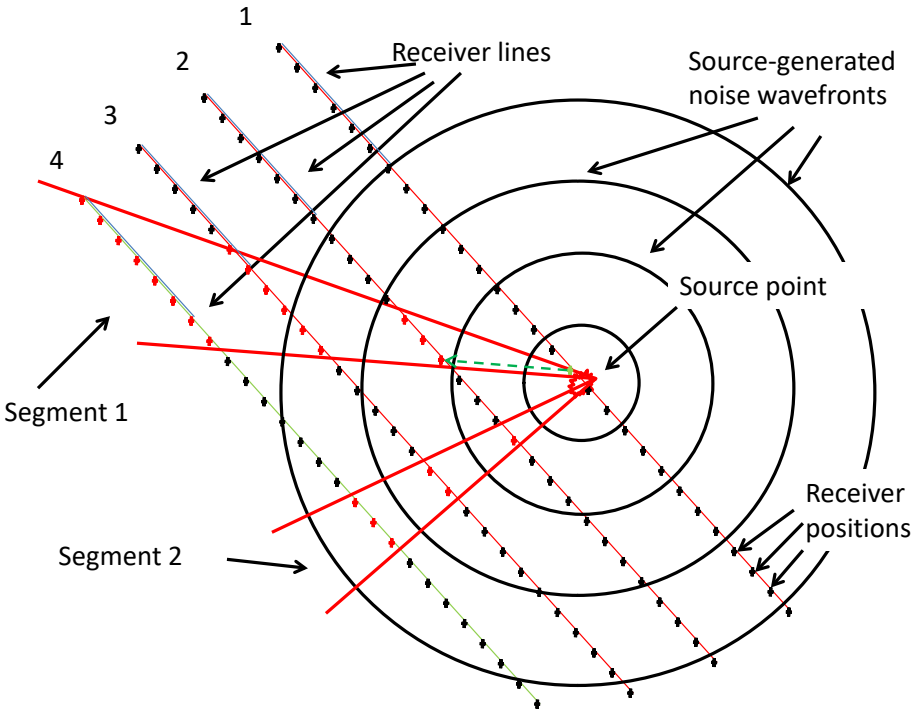

FIG. 3. Schematic showing that trace ensembles from different angular segments have greatly different offset distributions due to the combination of Cartesian geometry used in acquisition and polar geometry used to acquire bins.

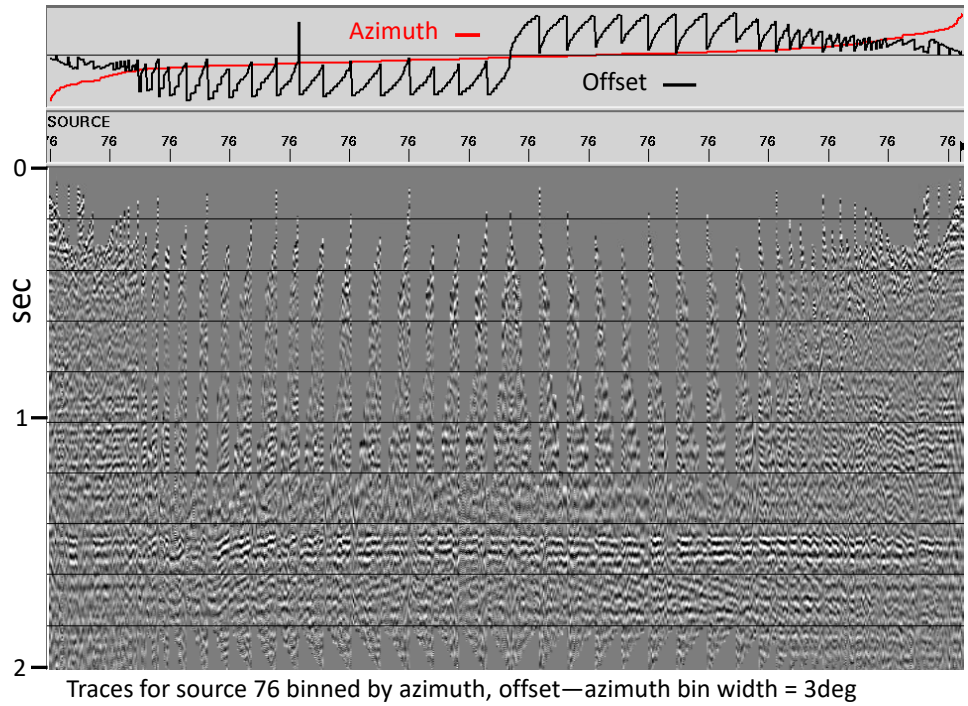

Traces for source 76 binned by azimuth, offset—azimuth bin width = 3deg

FIG. 4. Offset distributions in azimuth bins 3deg wide. Many bins have too few traces for meaningful raypath domain analysis.

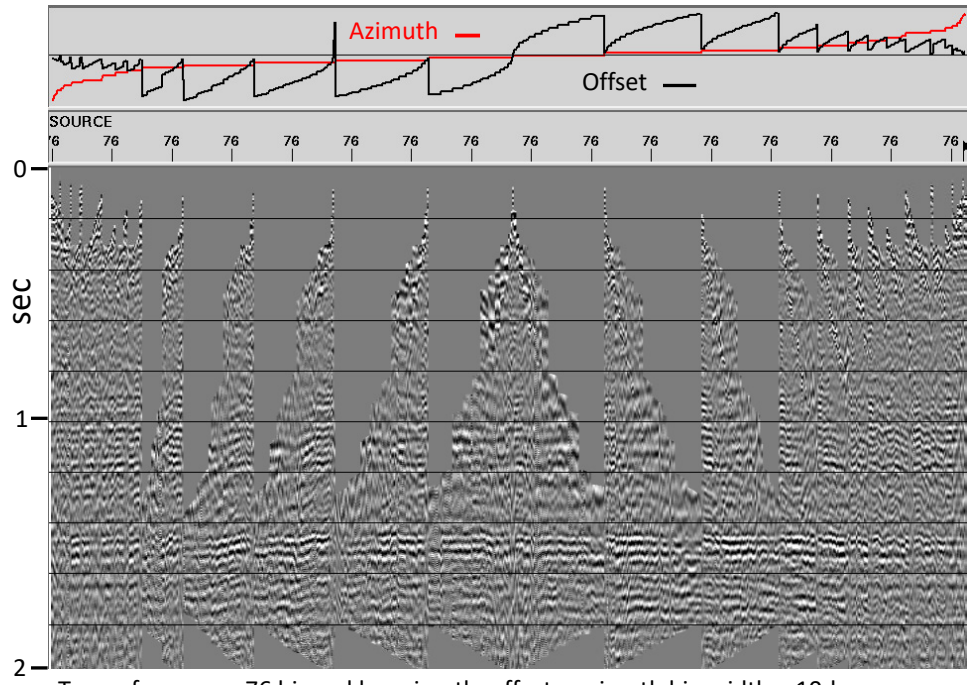

Traces for source 76 binned by azimuth, offset—azimuth bin width = 10deg

FIG. 5. Offset distributions in azimuth bins 10deg wide. Many bins still have too few traces, bin size varies widely.

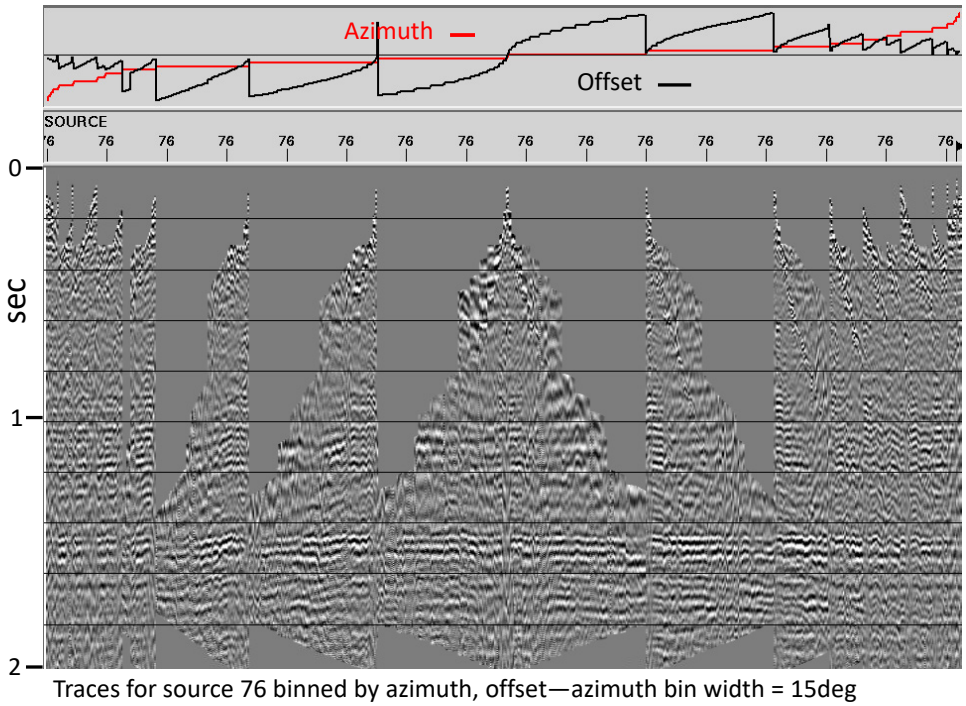

Traces for source 76 binned by azimuth, offset—azimuth bin width = 15deg

FIG. 6. Offset distributions for azimuth bins 15deg wide. Too many small bins.

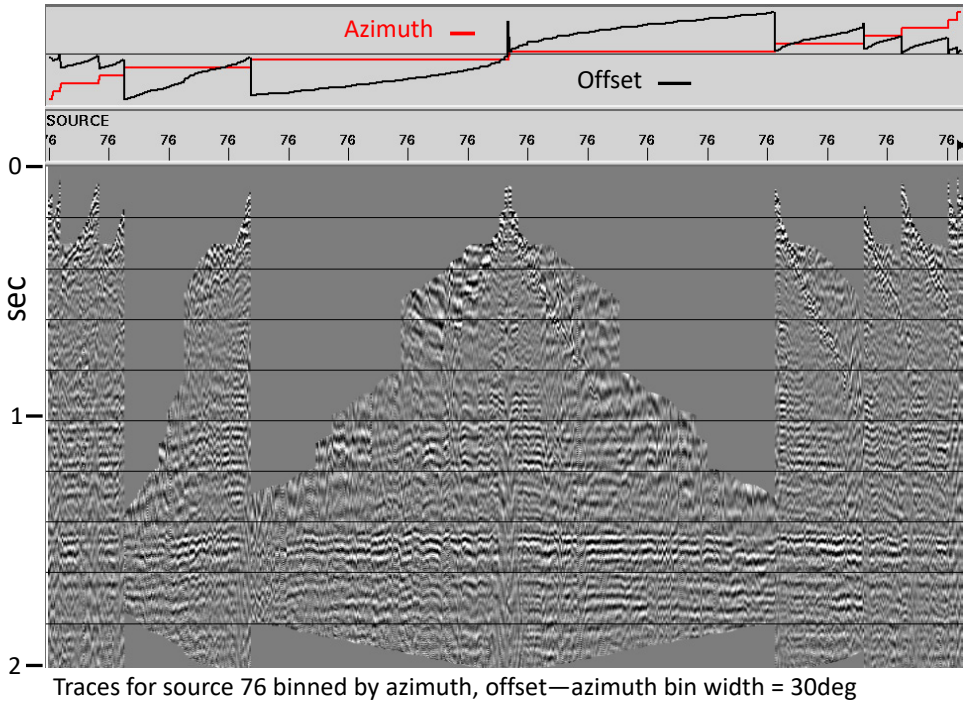

Traces for source 76 binned by azimuth, offset—azimuth bin width = 30deg

FIG. 7. Offset distributions for azimuth bins 30deg wide. Most ensembles now contain enough traces for meaningful raypath analysis, but bin size discrepancies still a concern.

Thus, there is an inevitable trade-off between strict adherence to the 2D criterion (coplanar raypaths) for a X-T-to-raypath transform and the trace distribution criteria (well-populated, uniformly distributed traces) which define a transform with a meaningful range of output raypath parameters. Even in Figure 7, which depicts the trace ensembles for 30deg-wide azimuth bins, the trace populations for a few azimuths are too small. One way to increase trace populations without increasing the departure of raypaths from the coplanar constraint is to append azimuth bins aligned with each other at 180deg. This creates propeller-shaped azimuth bins, as shown in Figure 8, whose trace distributions are shown in Figure 9, clearly an improvement over those in Figure 7.

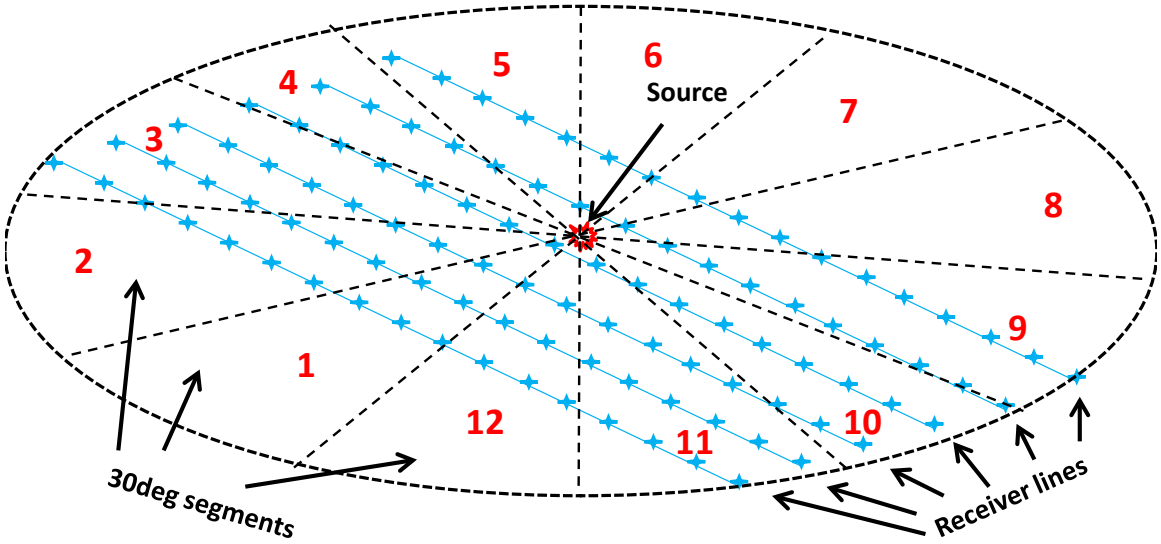

FIG. 8. Creation of 'propeller-shaped' bins to gather roughly coplanar azimuth values.

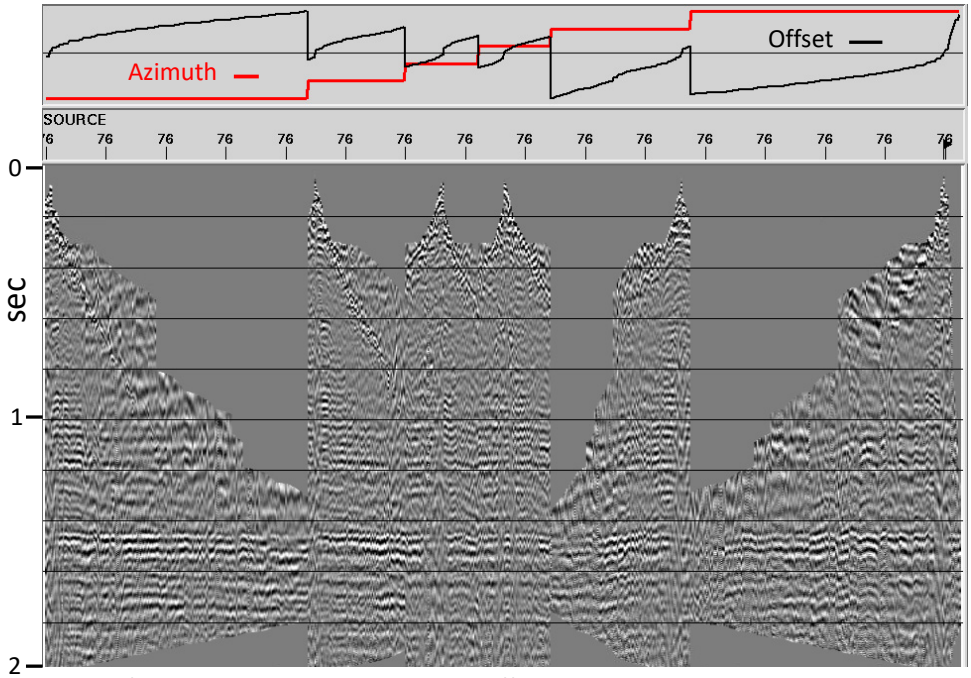

Traces for source 76 binned by azimuth, offset—azimuth bin width = 30deg, bins aligned by 180deg appended

FIG. 9. Offset distributions for 'propeller-shaped' bins depicted in Figure 8. These bins are well-populated, and offsets distributed very roughly uniformly.

Data dependence

It should be reasonably obvious from the previous discussions, and the figures shown, that choosing azimuthal bin parameters will always be dependent upon the particular 3D data set under consideration and its particular acquisition geometry. Data sets with higher CMP trace fold (more receivers per receiver line or more source positions) will allow the selection of narrower azimuth bins. Data sets with a very sparse source distribution may not be amenable to 3D interferometry at all, since the technique needs relatively uniform spatial sampling and high redundancy for reference wavefield estimation.

The data set

When we first considered the problem of extending raypath interferometry from two dimensions to three, we carefully surveyed our database to find a 3D seismic survey which fit the following criteria:

- Uncomplicated geological setting
- Uniform spatial sampling—no large gaps
- High quality data—good S/N
- Known surface-related statics of reasonably detectable size (at least 20-40ms)
- Small enough to process with reasonable turnaround (~1M traces)

Fortuitously, the 1995 Blackfoot 3D 3C survey (Lawton, 1996) fit all these criteria, and it had the further advantage that we could analyze not only the vertical component data for PP surface corrections, but also the radial component data for PS surface corrections (potentially much larger, and also more important). We thus chose to initially explore the vertical component Blackfoot 3D 3C data, as we first extended raypath interferometry into 3D. The results of this were described by Henley (2015), and Figures 4 thru 9 are repeated from that work. Since we chose to use our radial trace (RT) transform, with its inverse transform limitations, we did not attempt to construct CMP stacks after raypath interferometry, but only showed a comparison of a single source ensemble before and after correction (Figures 10 and 11). The distortion of the offset distributions caused by our RT inverse transform can be readily seen by comparing the offset distribution plots in these two figures; but the general increase in smoothness and coherence of the reflection events due to the raypath interferometry can also be seen.

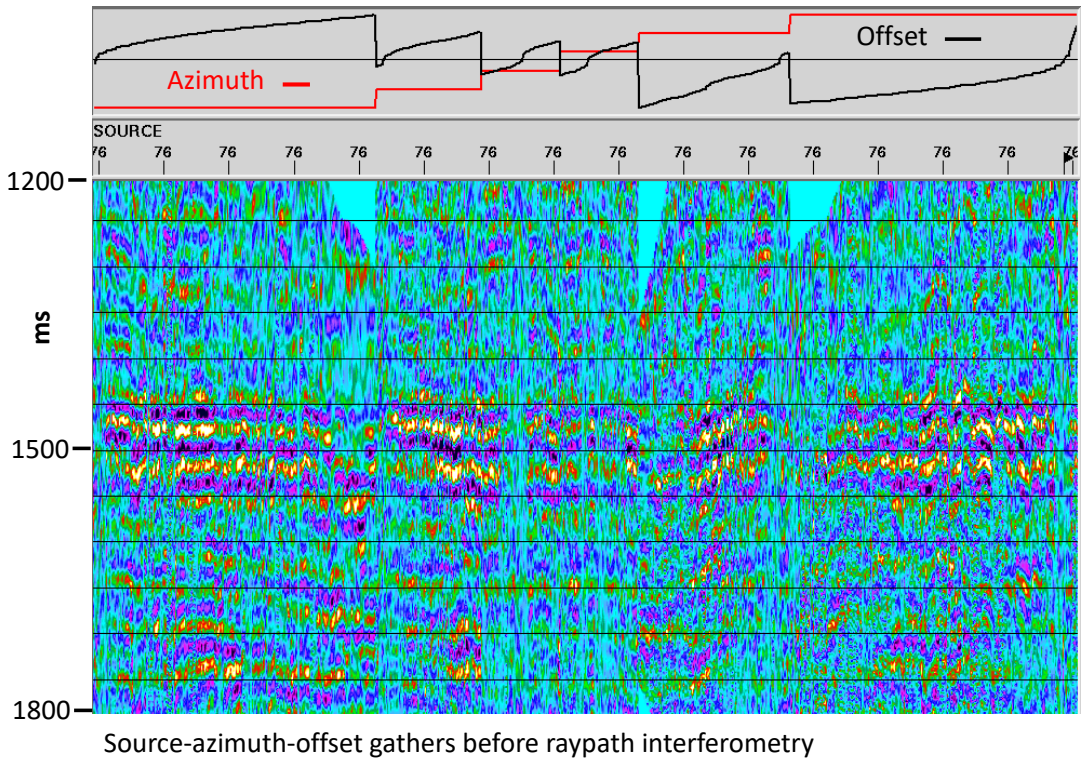

FIG. 10. Raw source-azimuth gathers (vertical component) before application of raypath interferometry. Note nonlinearity of offset distributions.

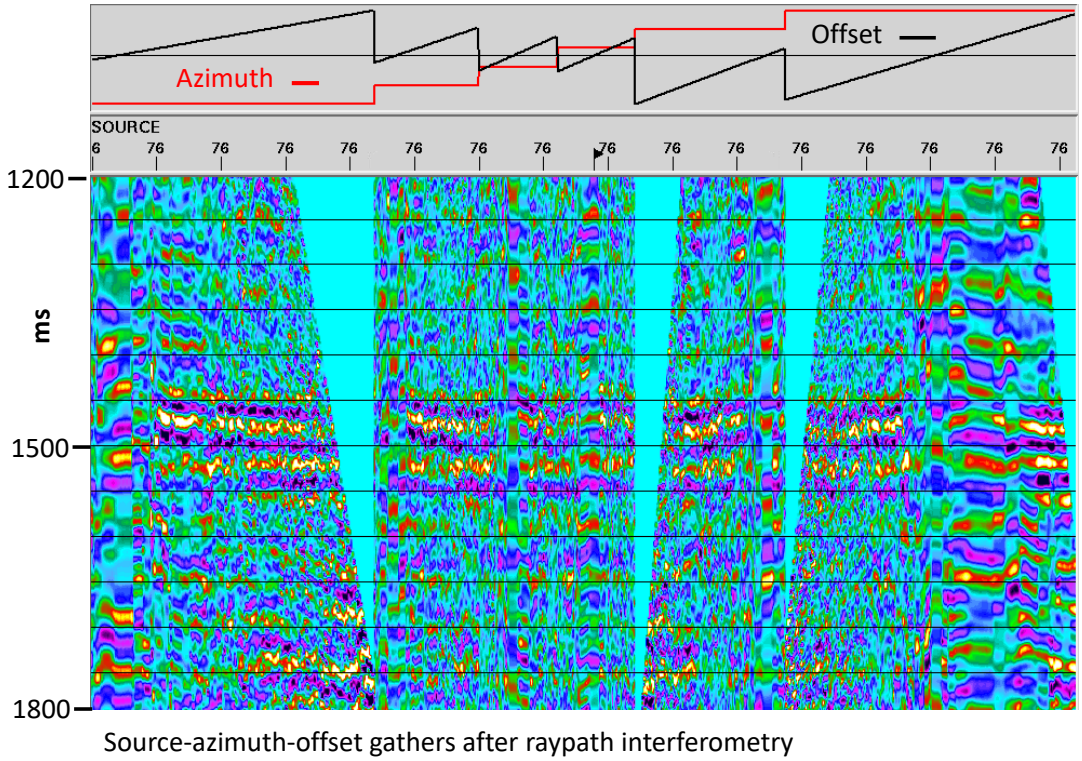

FIG. 11. Source-azimuth gathers (vertical component) after application of raypath interferometry. Note that the offset distributions have been forced to be linear...and the reflection events are thus distorted. The coherence and flatness of the main reflection events have been improved, however, demonstrating the effectiveness of raypath interferometry.

In the current study, we chose to continue our development by analyzing the PS data from the same 1995 Blackfoot survey, since surface corrections on the S-wave raypath side are typically much larger than any P-wave corrections, and often uncorrelated with them, as well. Furthermore, PS data typically have lower S/N and are correspondingly harder to process. We thus retrieved the radial component of the Blackfoot 3D 3C data, which had previously been created by rotating the inline and crossline components recorded in the field.

Processing

Since we had obtained reasonable results for the vertical component data (Henley, 2015), we chose to use the same processing flow to analyze the radial component, with the main difference being that the azimuth bins we chose were 45deg angular segments, and we did *not* append opposing segments to form propeller-shaped bins as with the vertical component data.

Since our existing RT transform was known to be unequal to the task of the forward/inverse operation when the input traces have a nonlinear distribution of source-receiver offsets (and is not easily repairable), we also investigated the use of a commercial Tau-P transform and its inverse. Our objective was to determine the viability of this alternate approach to the raypath domain, and to determine whether it should replace the RT transform in future work.

RESULTS

Using the RT Transform

The Blackfoot 3D 3C data were recorded in 1995 (Lawton, 1996), using a conventional 3D geometry consisting of a patch of parallel receiver lines into which many discrete source points were fired. Three components were recorded: vertical, inline horizontal (inline with the receiver line), and crossline horizontal. As part of the initial data processing, the amplitudes in the inline and crossline horizontal components were combined by trigonometric weighting to form two new components, the radial and transverse, in which the particle motion in the radial direction is along a line projected through the source, and particle motion in the transverse direction is perpendicular to that line. This process is known as 2D rotation. For our work, we began with the radial component from this initial processing operation.

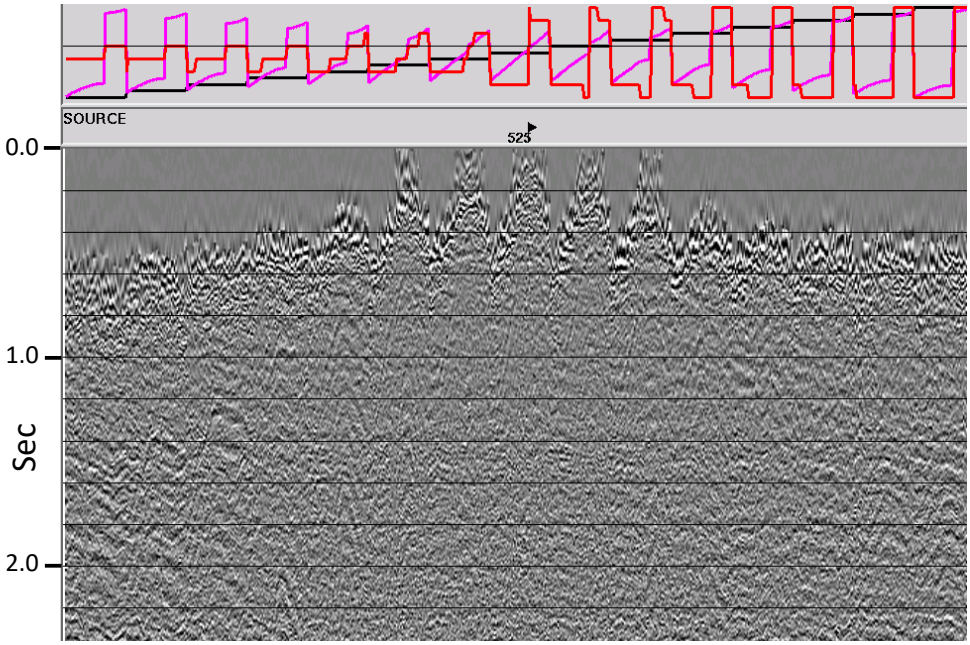

FIG. 12. Typical NMO-corrected source gather for the radial component of the Blackfoot 3D 3C survey, sorted by receiver line and offset. Receiver line plotted in black, offset in pink, azimuth bin in orange PS events are very faint and exhibit lots of statics.

Figure 12 shows a typical source gather for the radial component, consisting of traces from 15 receiver lines. NMO correction has been applied in order to make PS events relatively flat. The low S/N, however, makes it difficult to see much in the way of coherent events. For comparison, Figure 13 shows a typical source gather for the vertical (PP) component at a different source point (with the NMO uncorrected), where the reflection events are far more visible. We created a set of 45deg azimuth bins for the PS data, after some experimentation, and sorted all the radial component source gathers into azimuth-offset bins. Figure 14 shows the source gather of Figure 12 in this new trace order, and it is clear that ordering the traces by azimuth makes the PS (converted wave) events more coherent, and likely easier to analyze. It is also evident from this figure that there are large corrections needed to flatten the visible events.

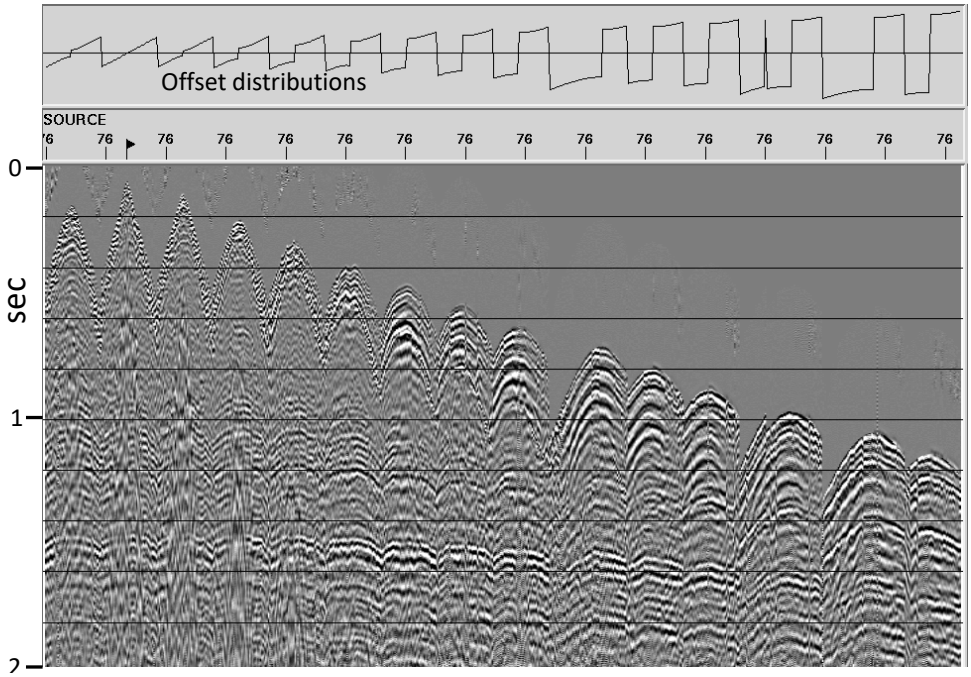

FIG. 13. Typical vertical component source gather, sorted by receiver line and offset. No NMO correction...reflection events are highly visible on all receiver lines.

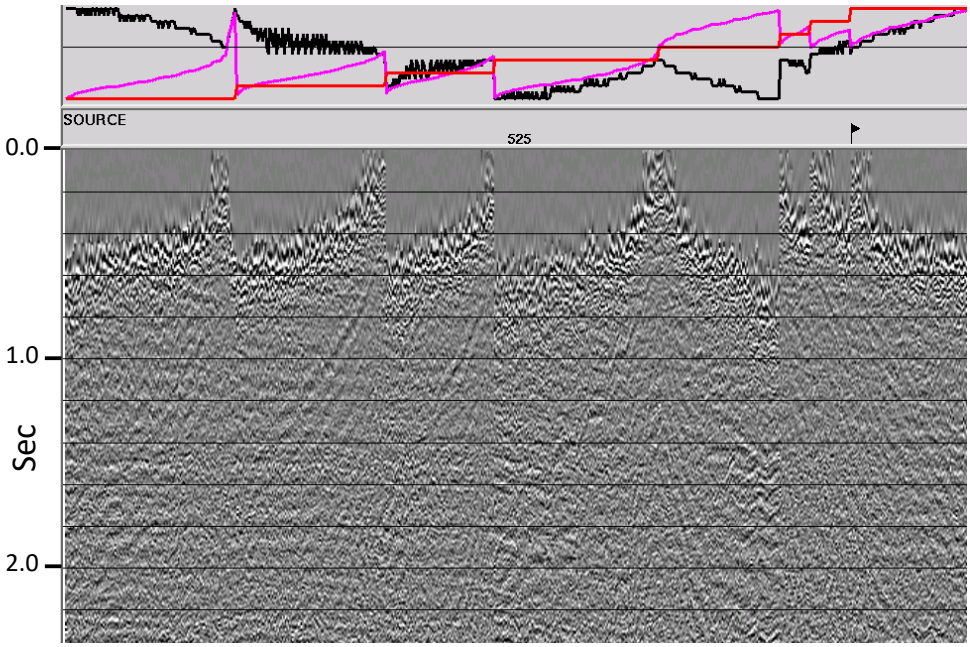

FIG. 14. PS source gather sorted by azimuth (orange plot) and offset (pink plot), with 45 degree azimuth bins. The PS events are more visible in this ensemble than in the original source gather in Figure 12

Following the procedure established while analyzing the vertical component (Henley, 2015), we applied the RT transform to the traces in each azimuth bin of each source gather, and sorted the resulting transforms by ray parameter, azimuth, and source. Figure 15 shows an example of one of the resulting common-ray-parameter gathers. This very

large ensemble contains about 60,000 live traces. Several of the azimuth bins are empty because they contain no raypaths with this particular ray parameter. If the selected ray parameter was positive, the empty azimuth bins in Figure 15 would be populated, but some of the others would be empty. This is a consequence of designating the azimuth in terms of the vector raypath direction from the source to the receiver. If we had chosen to combine azimuth bins 180deg apart as in Henley (2015), a gather similar to that in Figure 15 would have no empty bins, since raypaths of mirrored near-surface angles would have all been included.

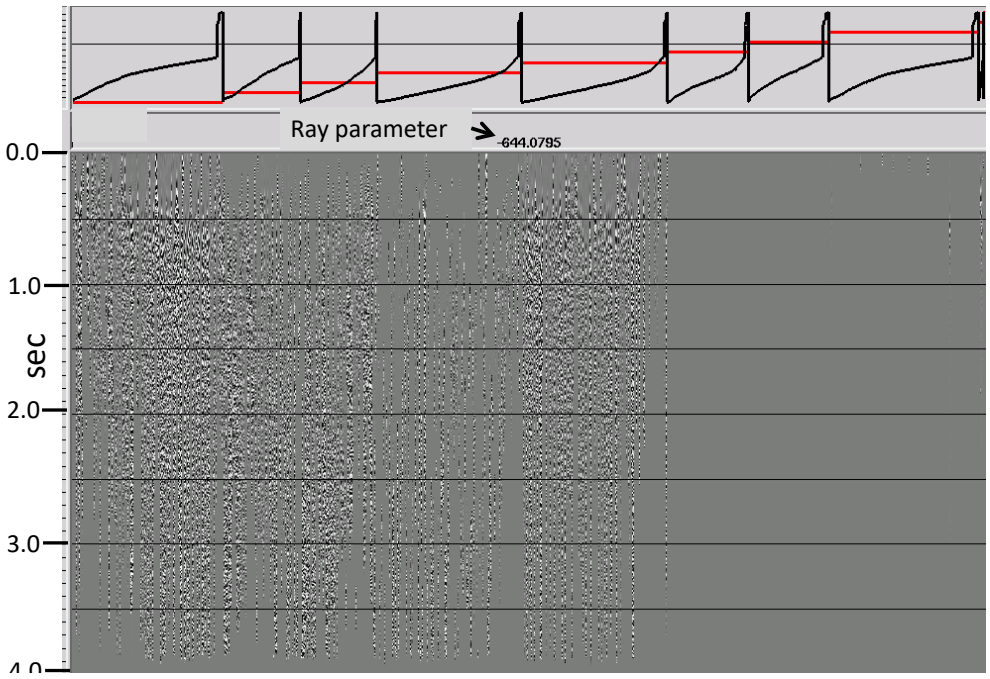

FIG. 15. Common-ray parameter ensemble. Several azimuth bins (red plot) are empty because the raypath directions to which they correspond are positive, and the common ray parameter for this ensemble is negative.

In our earlier work (Henley, 2015), we showed that the reference wavefield for performing raypath interferometry can be obtained by enforcing smoothness and continuity along two different directions in the collection of common-raypath trace gathers, and that the smoothing directions need not be orthogonal. Hence, we applied trace mixing and eigenvector filtering to the common-raypath gathers, first in the azimuth direction within common-source, then in the source direction over common-azimuth. Figure 16 is the common-ray-parameter display of this twice-smoothed 'reference wavefield' estimate for the particular ray parameter -1505m/s. While some events in this gather may not seem particularly smooth, it should be emphasized that within each azimuth bin there are over 7000 traces, so evident 'roughness' in the events is greatly exaggerated by the compressed horizontal scale.

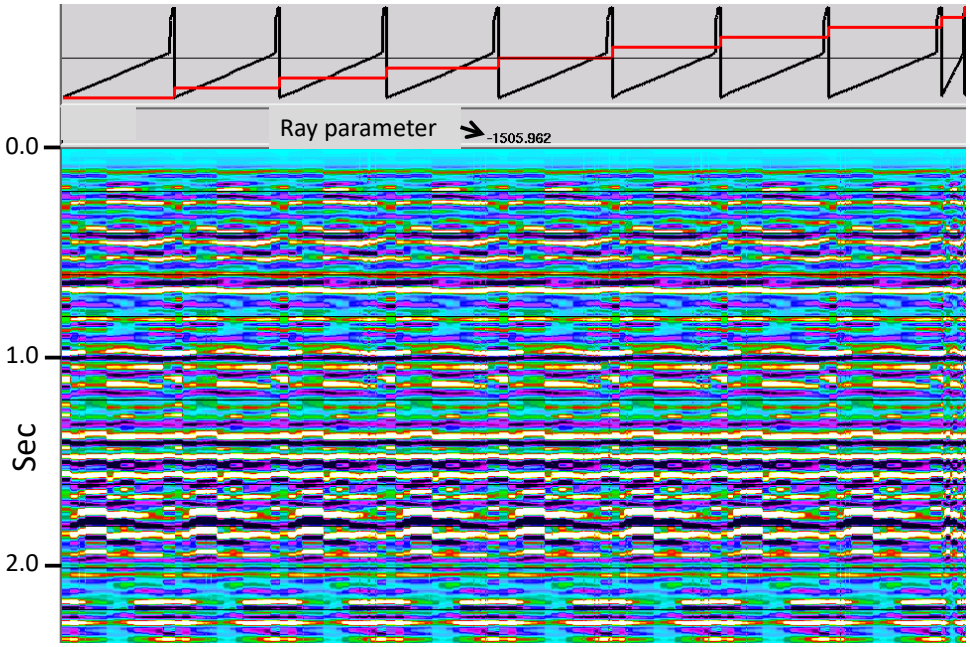

FIG. 16. Common-ray parameter ensemble (reference wavefield), smoothed first over azimuth (red plot), then source location (black plot). The events may not seem particularly smooth because of the horizontal compression (about 7000 traces in each azimuth bin)

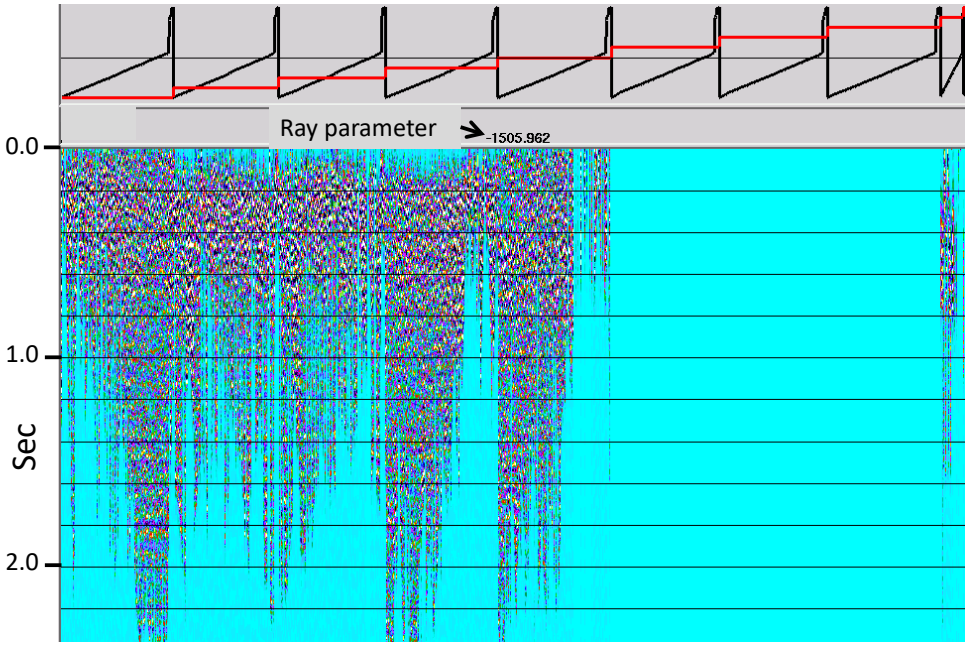

FIG. 17. Common-ray parameter ensemble of raw traces to be matched to the corresponding traces in the reference wavefield ensemble in Figure 16.

Figure 17 shows the raw common-ray-parameter panel for the ray parameter -1505, and Figure 18 shows this panel with its traces alternately interleaved with those of the corresponding reference wavefield panel of Figure 16. Figure 19 is a zoom of a very small portion of the trace pairs displayed in Figure 18, where we can see the similarity

between the PS events on the raw common-ray-parameter panel and the reference wavefield traces, but also the time-shift/phase differences between them. It is the cross-correlation of the trace pairs in all the panels like Figure 18 that creates the 'surface function' estimates needed to apply surface corrections.

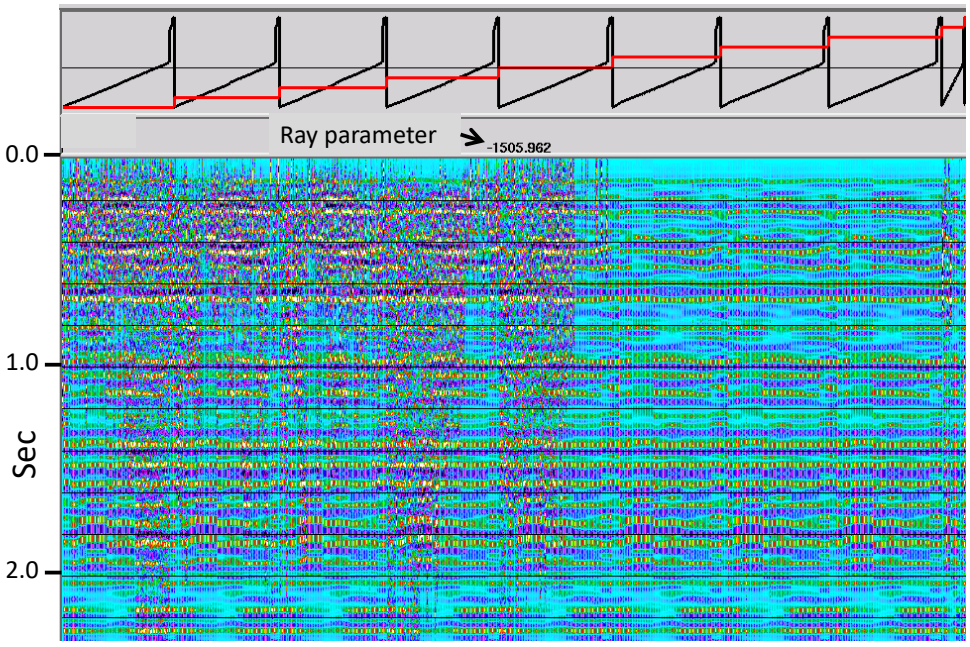

FIG. 18. Traces of Figure 16 and Figure 17 matched and interleaved for cross-correlation and estimation of surface functions.

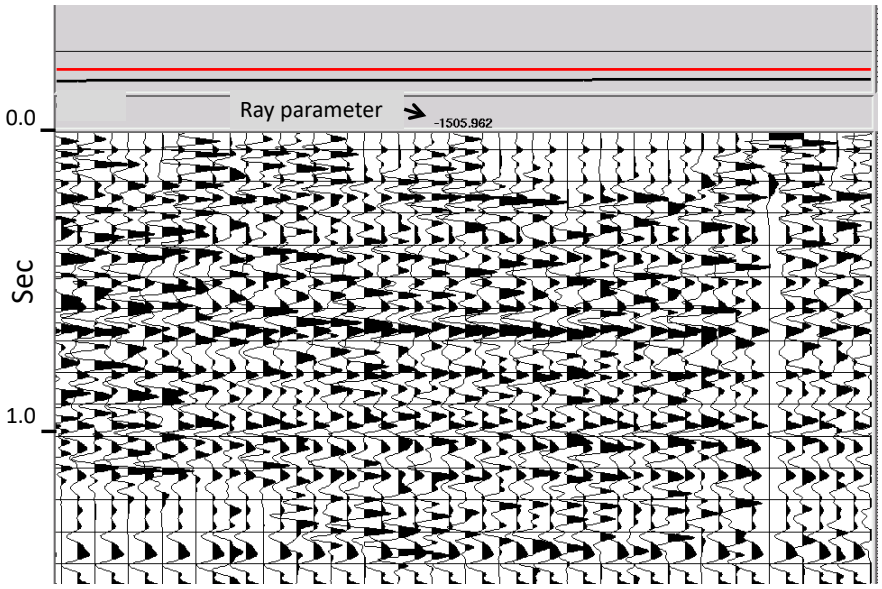

FIG. 19. Zoom view of a small portion of the traces in Figure 18. Each pair of traces consists of a raw trace and a reference wavefield (pilot) trace. Cross-correlations between the traces in each pair are the basis for the 'surface function' estimates, which are just 'conditioned' cross-correlation functions.

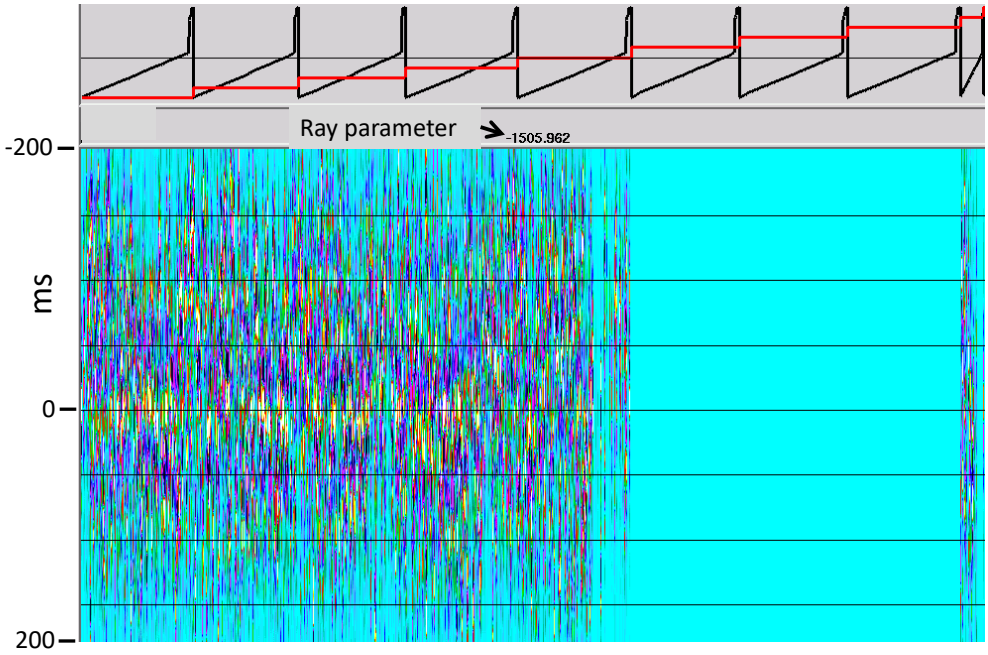

FIG. 20. Surface functions created from the interleaved common-ray-parameter ensemble in Figure 18.

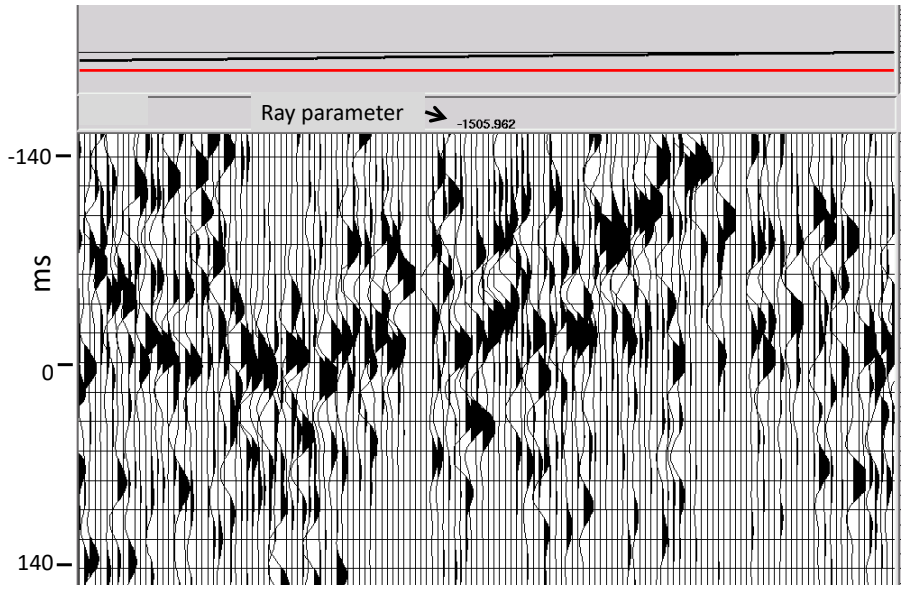

FIG. 21. Zoomed view of small portion of the surface functions in Figure 20.

Figure 20 displays the surface functions estimated for the common-ray-parameter panel of Figure 17, and Figure 21 shows a zoom of a small portion of these functions. While many of the surface function 'peaks' are near the zero-shift position, many depart significantly, denoting significant time/phase shift between the raw traces and the reference wavefield.

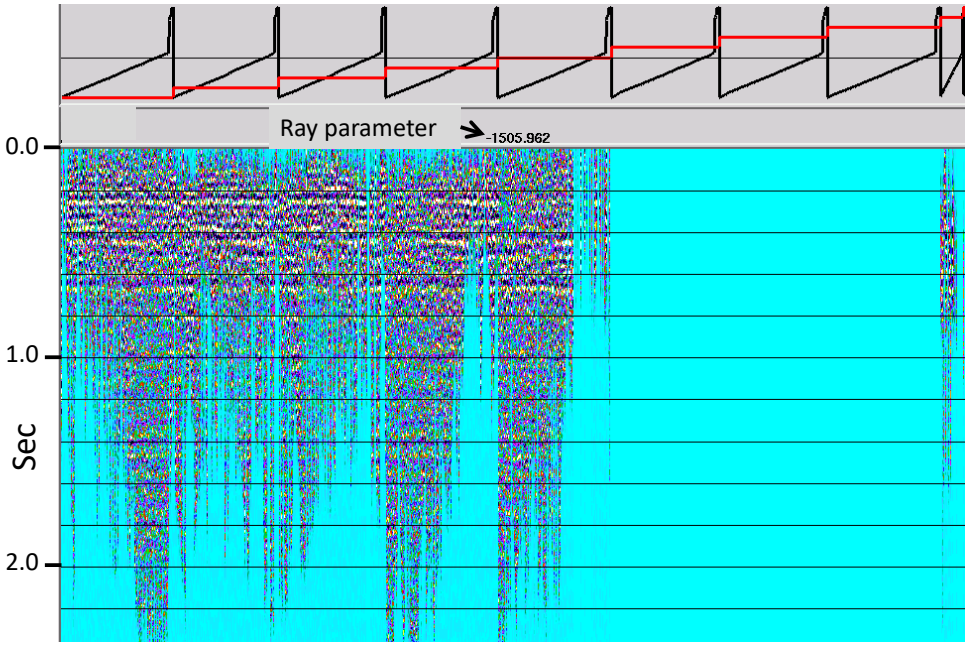

FIG. 22. Common-ray-parameter ensemble from Figure 17 after being corrected by deconvolving the surface functions shown in Figure 20. Events are much more coherent and flat in this Figure than they are in Figure 17. Most of the apparent events in this ensemble are shallow, since this particular ray parameter captures rays that do not penetrate very deeply.

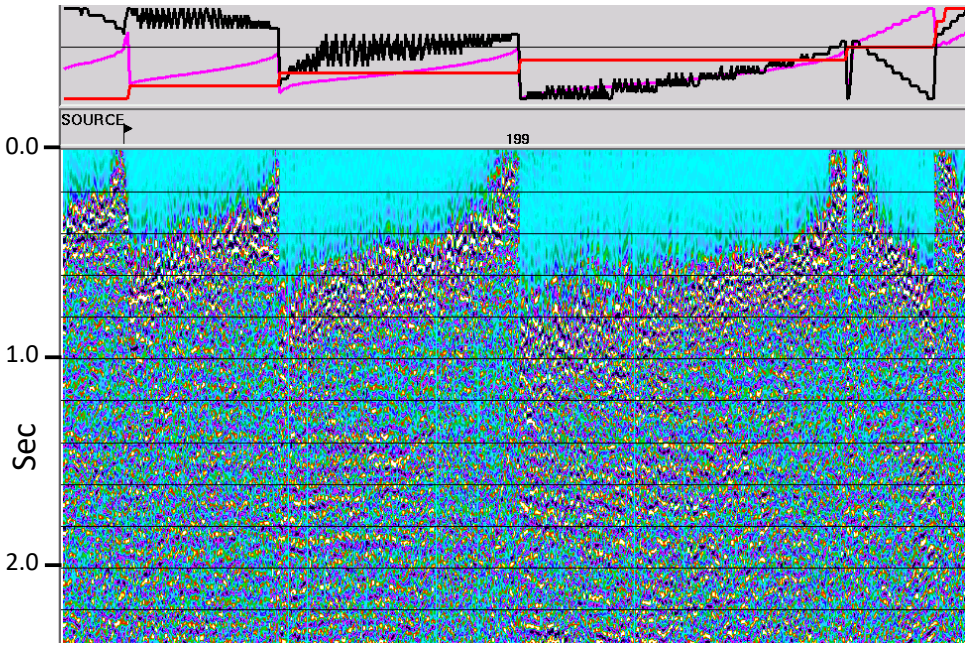

FIG. 23. Uncorrected common-azimuth gather for source point 199. Note nonlinear offsets (pink plot). Events visible, but show lots of time and character variations.

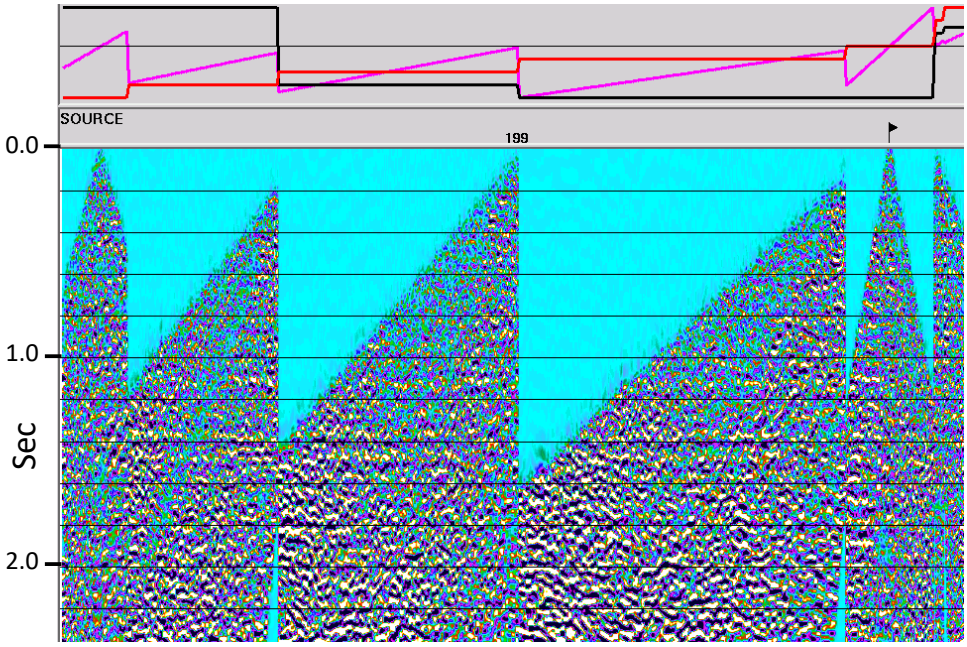

FIG. 24. Corrected common-azimuth ensemble for source 199. Azimuth bins plotted in orange, offsets in pink. Offsets have been linearized by the RT inverse transform.

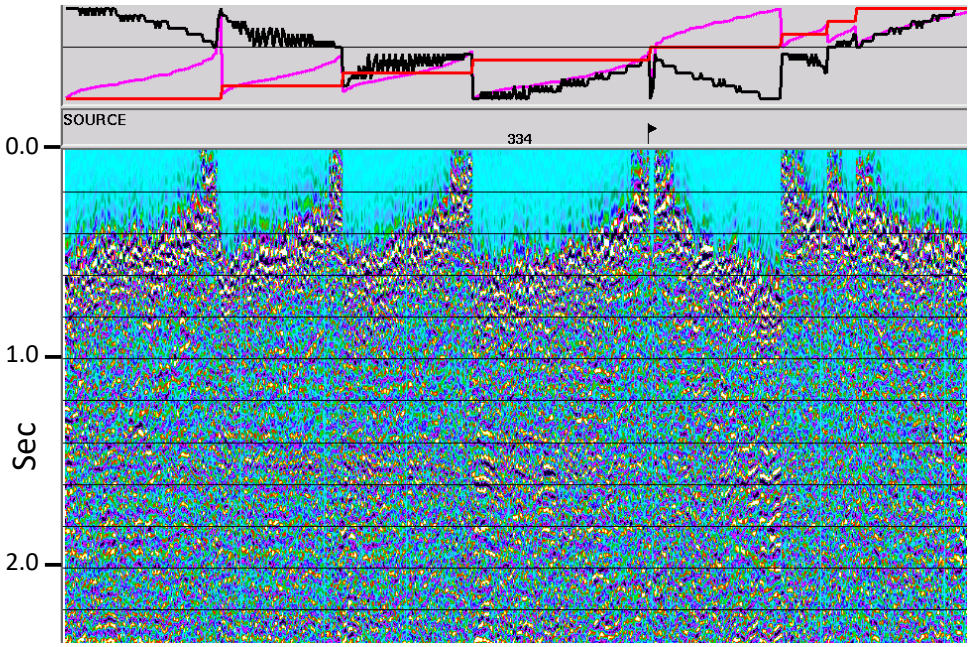

FIG. 25. Raw common-azimuth ensemble for source point 334, corresponding to the raw ensemble.

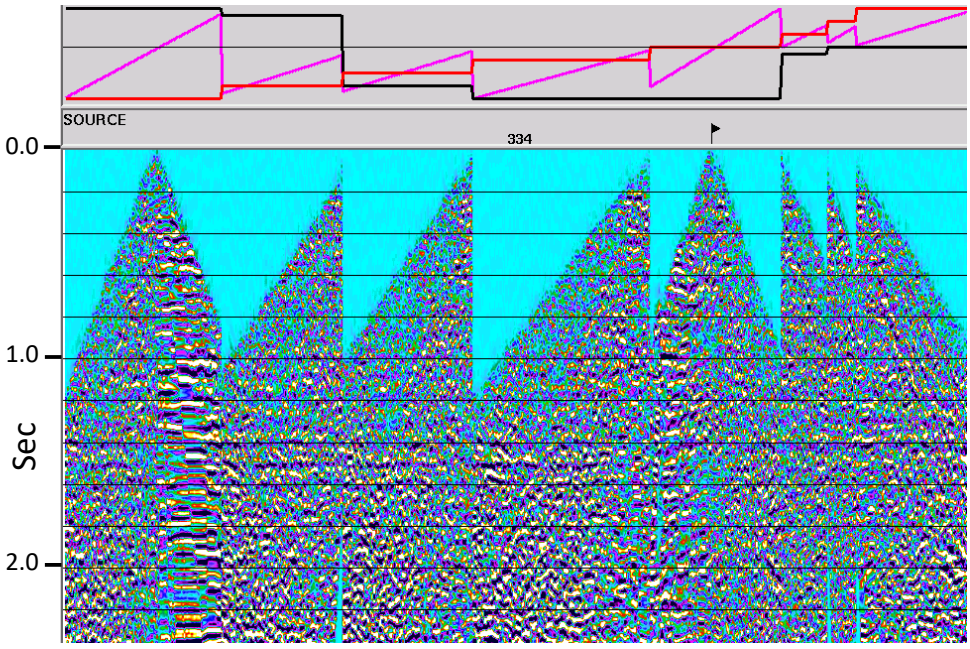

FIG. 26. Corrected common-azimuth ensemble for source point 334. Events have been flattened and coherence improved, but offsets (pink plot) have been linearized.

When we apply the surface functions created from the common-ray-parameters, results like those in Figure 22 are the result. Note the greatly improved event flatness and coherence on this panel, compared to the input panel in Figure 17. To evaluate this result back in the native X-T domain, we first re-sorted the traces into source-azimuth gathers, then applied the inverse RT transform. Figure 23 shows the raw common-azimuth panel for source number 199, while Figure 24 is the same panel after correction. The comparison is not exact, since the original source-receiver offset values, which can be seen to be nonlinear in the trace header plot in Figure 23 are forced to be linear by our inverse RT transform operation. Figures 25 and 26 are the uncorrected and corrected source gathers for source point 334, respectively, and similar distortions are present. Importantly, however, the PS events, which can be seen faintly in both Figures 23 and 25, are seen to be significantly flatter and more coherent in the corresponding figures 24 and 26.

Using the Tau-P Transform

Motivation

When we first began using the RT Transform for coherent noise attenuation and other processing functions (Henley, 1999), we developed a transform module in ProMAX which was designed to accommodate only 2D data. As such, it was intended to accept source-receiver offsets which were linear, or nearly so. This assumption facilitated a shortcut with respect to trace header storage and retrieval between forward and inverse transforms...we used relatively unused trace headers to store the number of traces in the original gather, the first and last offset values, and the first CMP and CMP increment. This was necessitated by the fact that an RT Transform typically has a different number

of traces than the original X-T panel, and therefore cannot store the original trace headers one-for-one in the transform traces. Storing the minimal headers listed above, in the header array for *each* RT trace, however, the inverse transform operation can use these values to linearly interpolate the offset values into the inverse transform traces, and to recreate the CMP values, as well. As long as the offset values in the input panel do not depart significantly from a linear distribution, this approximation is acceptably accurate.

In 3D, however, source-receiver offset values are no longer linear. For any receiver line which is not collinear with the source position, the offsets will be hyperbolically distributed, the departure from linearity increasing with the perpendicular offset of the source from a given receiver line. It is this departure which leads to the offset distortions seen in Figures 23 and 25; and it is what prevents us from doing more than a visual comparison between Figures 23 and 24 and between 25 and 26. The RT inversions are too inaccurate to use for CMP stacking and imaging.

Cova et al (2014a, 2014b, 2015) have shown that a good alternative transform for moving from the XT domain to the raypath domain is the Tau-P Transform. We had initial misgivings about its inexact inverse, due to limitations in aperture, but we show below that with proper choice of parameter, the errors due to aperture limits are small relative to the offset errors in our RT Transform. The big advantage, practically speaking, is that the Tau-P transform and its inverse are commercially developed algorithms, and they properly post the necessary trace headers in a software package database for retrieval during the inverse transform. This means that the inverse transform output trace ensemble will always have exactly the same traces and trace headers as the input X-T ensemble. Furthermore, a set of Tau-P transforms can be sorted into a different trace order, the traces modified by further processing, and the traces re-sorted into Tau-P gathers, and the original trace headers will still be properly restored upon inversion of the Tau-P ensembles. The only inaccuracies in the forward/inverse Tau-P operation, then, will be due to the aperture limitations.

Difficulties

As we quickly discovered, there is one additional feature of the Tau-P transform which creates difficulties when using it on a 3D data set; it is not a compact transform, typically creating a Tau-P ensemble requiring from one to two orders of magnitude more storage than the input X-T ensemble. For example, Figure 27 shows a Tau-P transform of a 631 trace azimuth bin ensemble whose traces are 2400ms in length. The chosen aperture (required for acceptable data fidelity) leads to a transform ensemble more than 15 times as large (37,000ms trace length). If we were to limit the aperture to approximately half of that displayed (by choosing minimum and maximum slowness limits of about half of those displayed), the required storage would also reduce by half; but the data fidelity of the inverse output ensemble would be unacceptably compromised.

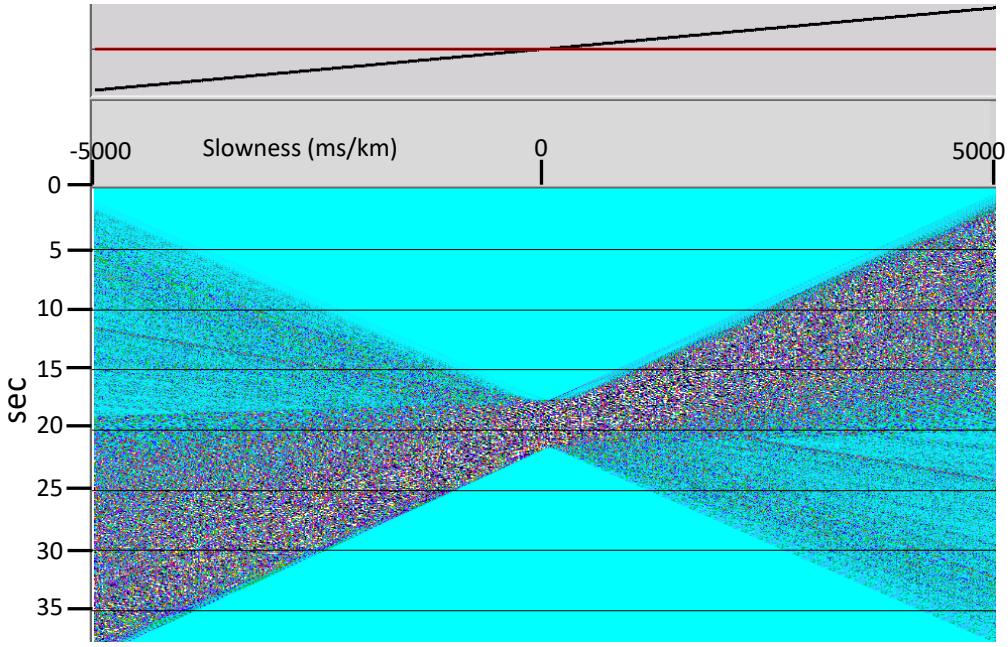

FIG. 27. Tau-P transform of one 631-trace azimuth bin ensemble whose traces are 2400ms long. The Tau-P slowness aperture for this transform is -5000sec/km—5000sec/km to maximize data fidelity. Obviously, the required storage for such a transform is problematic, since it requires approximately 15 times as much as the input ensemble.

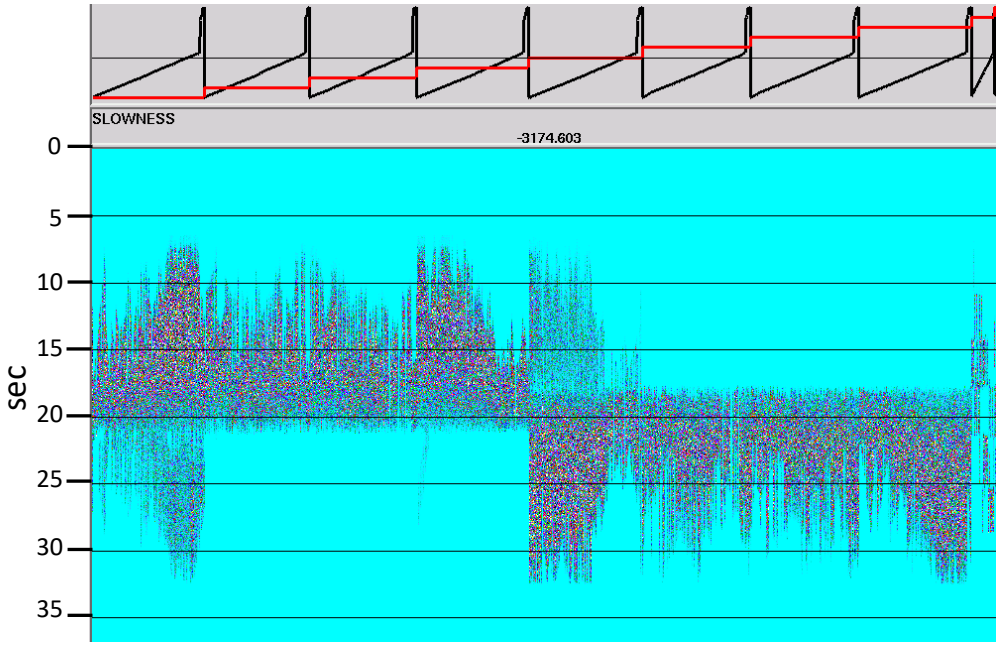

FIG. 28. Common-ray-parameter panel for the slowness value of -3174sec/km.

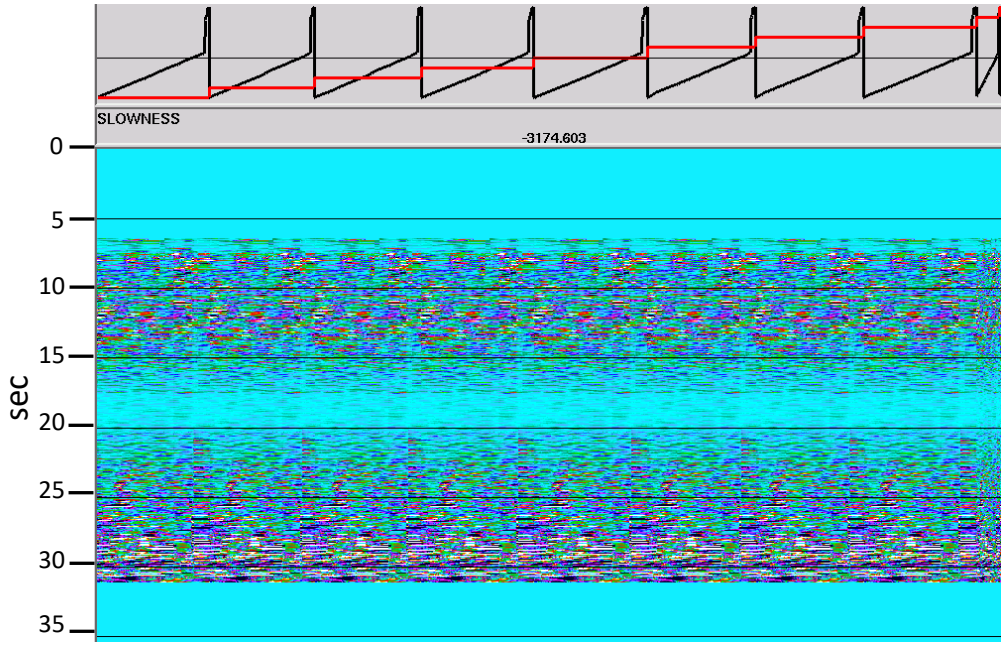

FIG. 29. Typical common-ray-parameter ensemble from the reference wavefield, smoothed in the azimuth and source location directions.

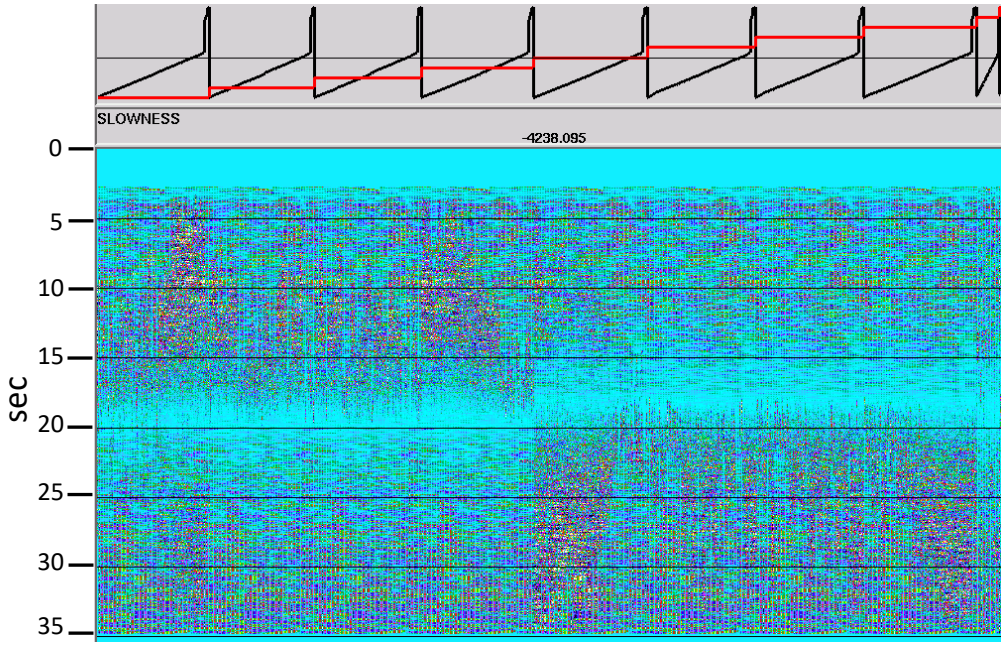

FIG. 30. Common-ray-parameter panel of interleaved trace pairs from the raw data and reference wavefield ensembles. Each trace pair is used to estimate a surface function.

We used the Tau-P parameters demonstrated in Figure 27 to transform the radial component Blackfoot data, and we show one common-ray-parameter panel in Figure 28 for the slowness value of -3174sec/km. The reference wavefield panel corresponding to this panel is featured in Figure 29, and an interleaved panel for a different slowness in Figure 30. The surface functions estimated by pairwise cross-correlation of Figure 30 are

displayed in Figure 31. While on this scale, the correlations all appear to be closely centred on zero shift, the zoom view in Figure 32 shows that this is far from the case.

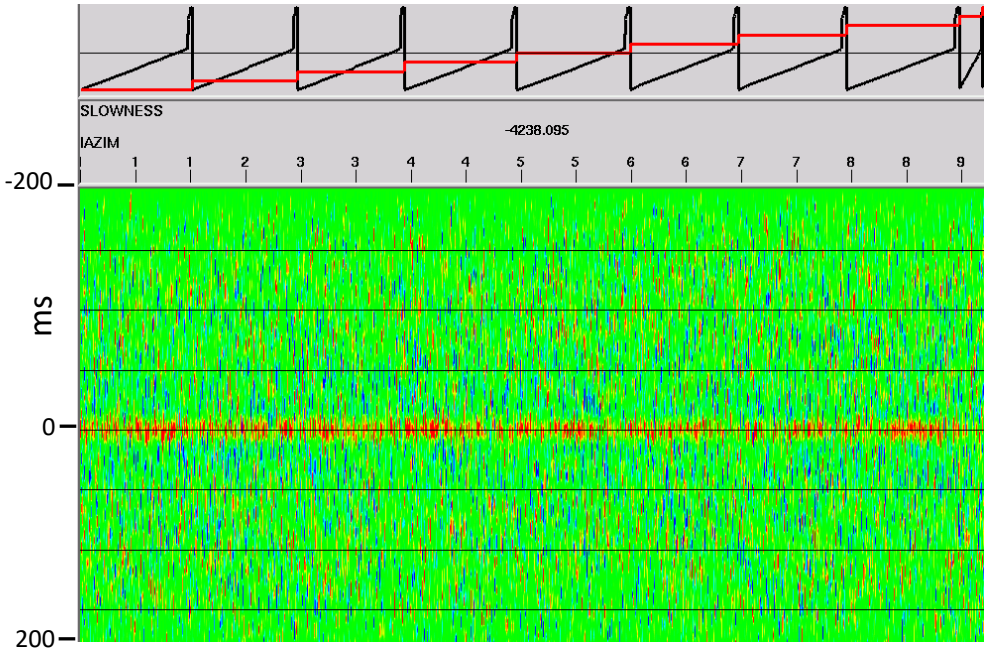

FIG. 31. Surface functions estimated from the trace pair panel in Figure 30. On this scale, the functions appear to be mostly centred on zero...

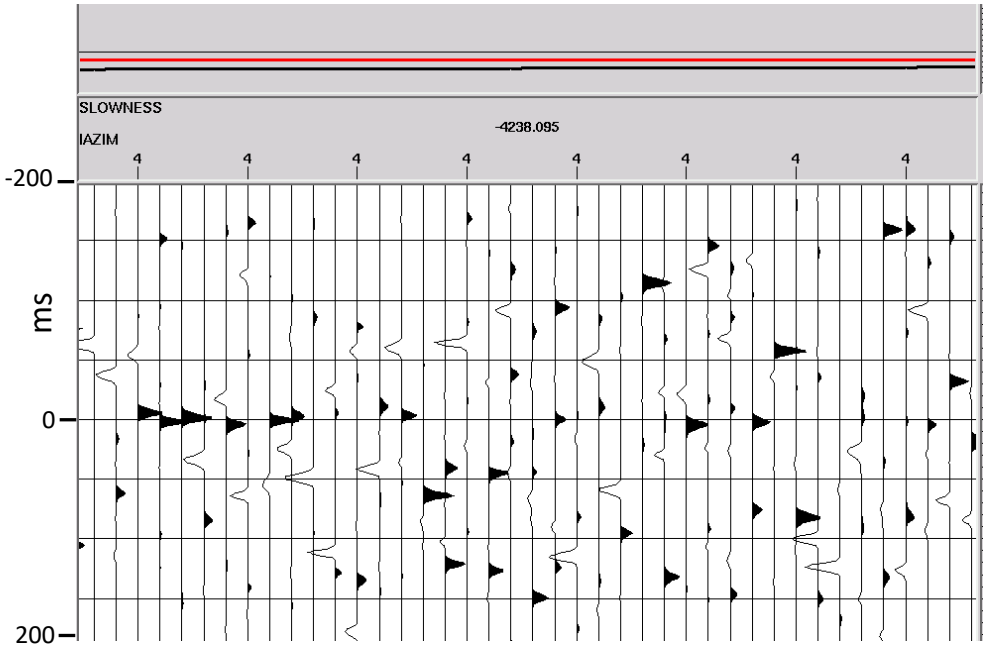

FIG. 32. Zoomed view of a small part of the surface functions in Figure 3. On this scale, the functions contain lots of non-zero shifts and phase changes.

While, in theory, we should be able to apply all surface functions to the common-ray-parameter ensembles of the entire 3D data set, current storage limitations allowed us to

proceed only as far as application of corrections to the common-ray-parameter ensembles, but not to re-sorting and inversion back to X-T. Hence, as proof of principle, we present Figure 33, which is a small portion of a common-ray-parameter ensemble before correction, and Figure 34, the same common-ray-parameter portion after correction.

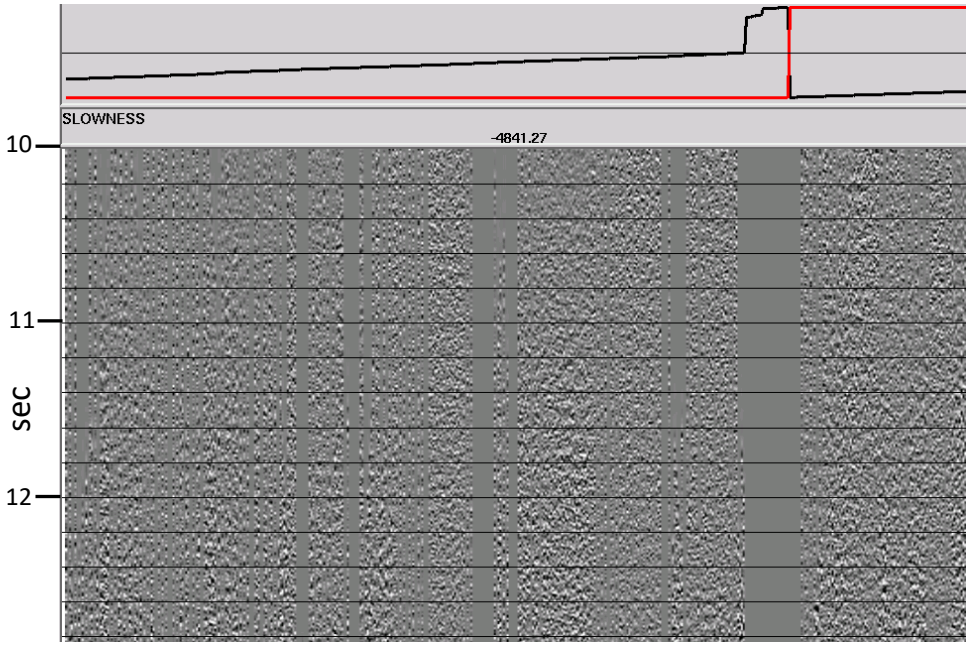

FIG. 33. Small portion of common-ray-parameter ensemble before raypath interferometry.

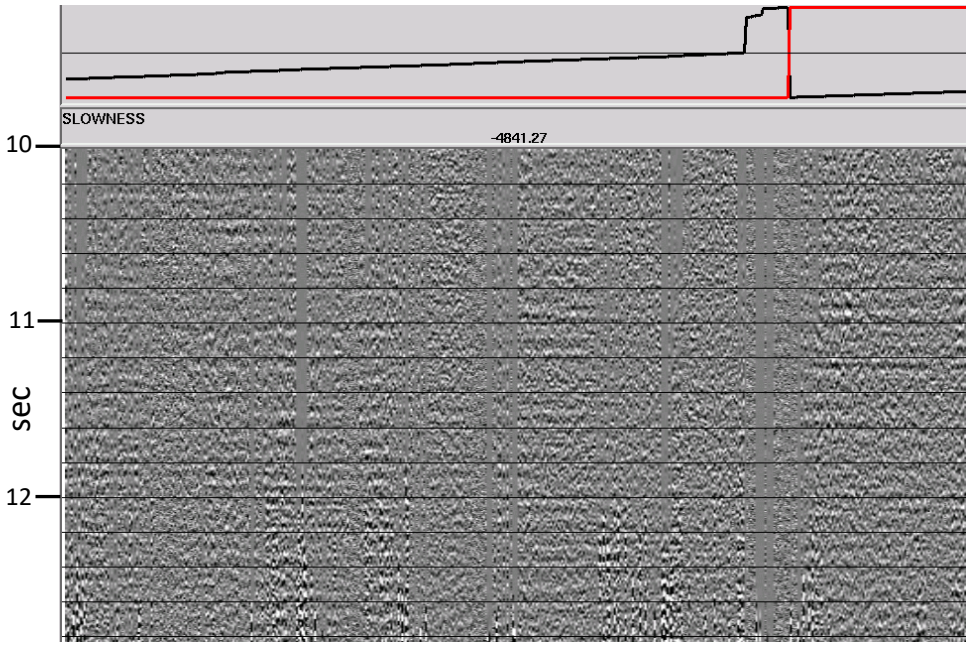

FIG. 34. Same traces as in Figure 33, after raypath interferometry.

Likewise, Figures 35 and 36 are before and after views of a different portion of the same common-ray-parameter ensemble. It is clear in both of these comparisons that the seemingly random events of the uncorrected ensembles have been successfully corrected.

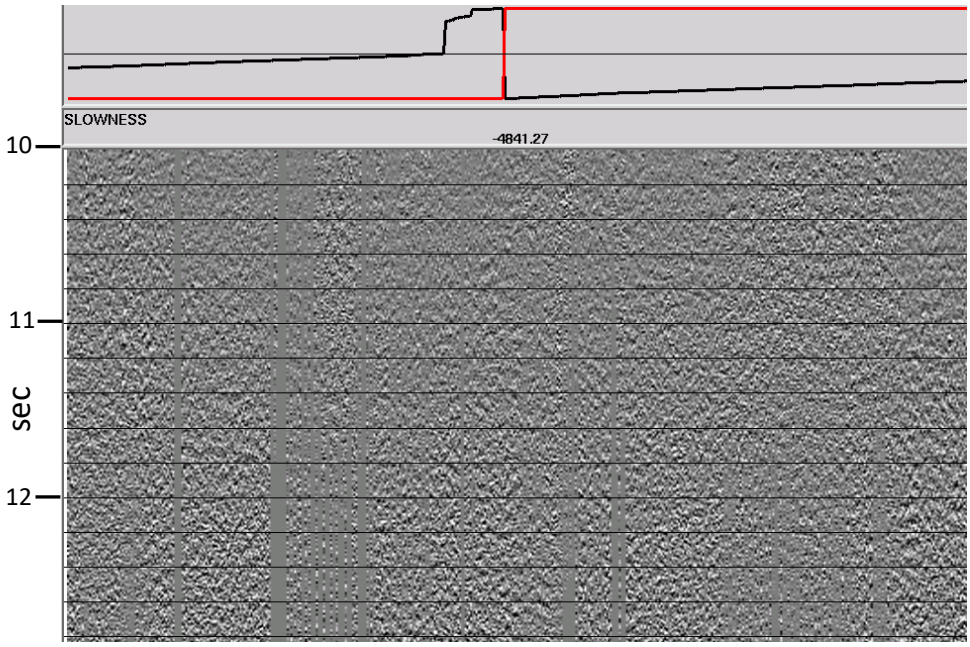

FIG. 35. Another small portion of the same common-ray-parameter ensemble as Figure 33.

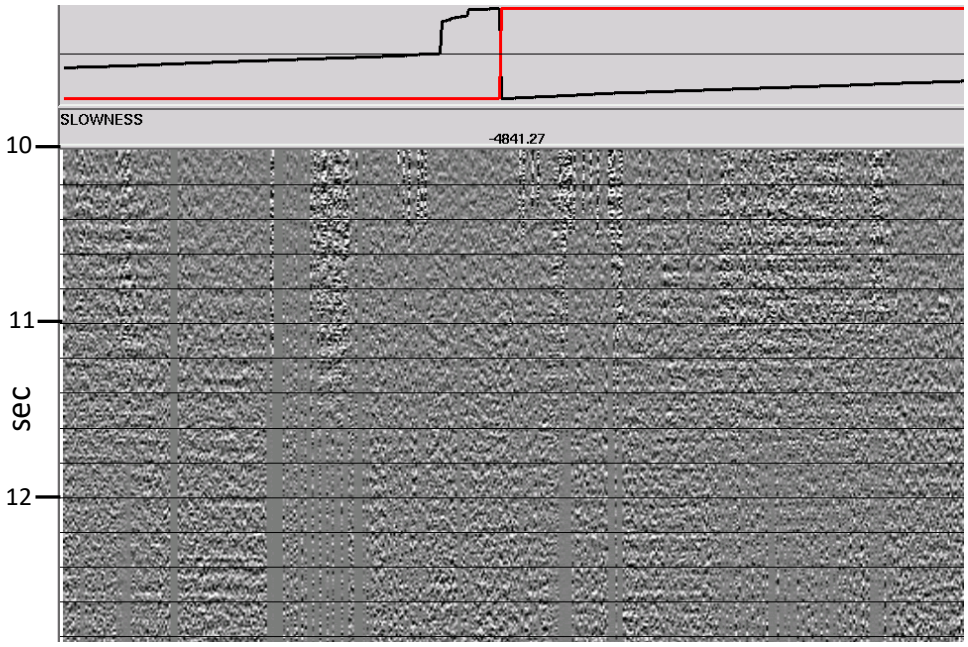

FIG. 36. Same traces as Figure 35, after raypath interferometry.

Comparative transform fidelity

In order to give a better intuitive feel for the respective limitations of the RT and Tau-P transforms, we chose first a common-azimuth bin ensemble from one source gather in the Blackfoot data, shown in Figure 37. The offsets, plotted at the top of the figure, are very closely linear with trace number. When we apply the RT transform and its inverse, with a mild bandpass before inversion, the result is shown in Figure 38. As can be seen, the data retain their full fidelity, with a small amount of amplitude leakage into the dead trace (arrow), due to the interpolation in the RT transform and its inverse, and the forced linearization of the output offset values. The same ensemble is shown in Figure 39 after forward and inverse Tau-P transform, with transform parameters chosen to maximize lateral resolution. In comparison with Figure 38, this transform pair preserves data fidelity just as well. There is no leakage into the dead trace, since each output trace is an independent back-projection to a precise offset value, with no forced linearization between them. For this input ensemble, with its nearly linear offset distribution, either transform could be used equally effectively. The RT transform requires far less storage than the Tau-P transform, but the Tau-P transform retains exact offset values, regardless of their linearity.

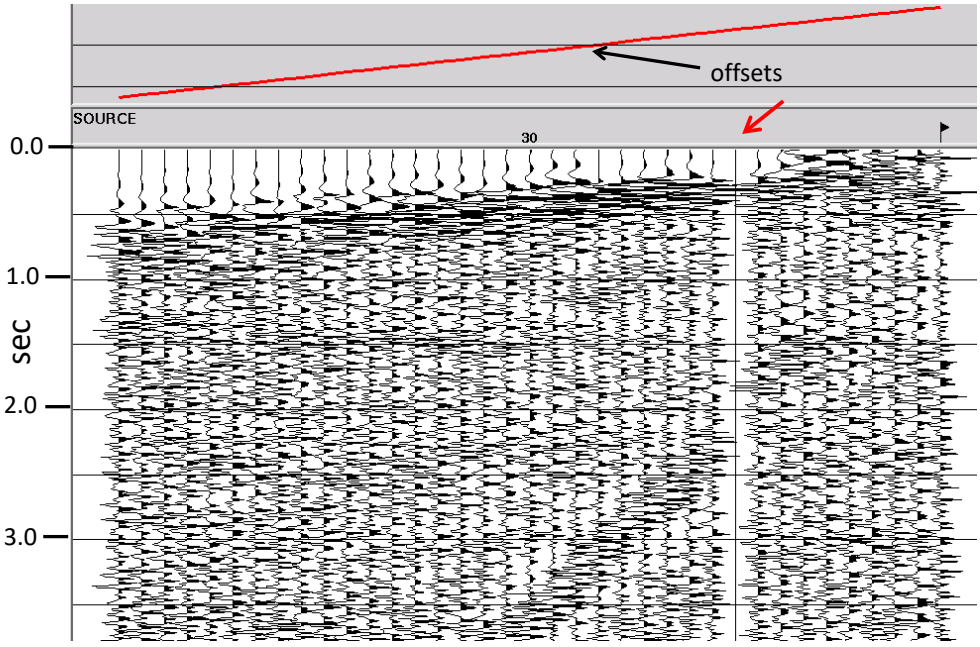

FIG. 37. Common-azimuth bin ensemble with nearly linear offset distribution. Note the dead trace.

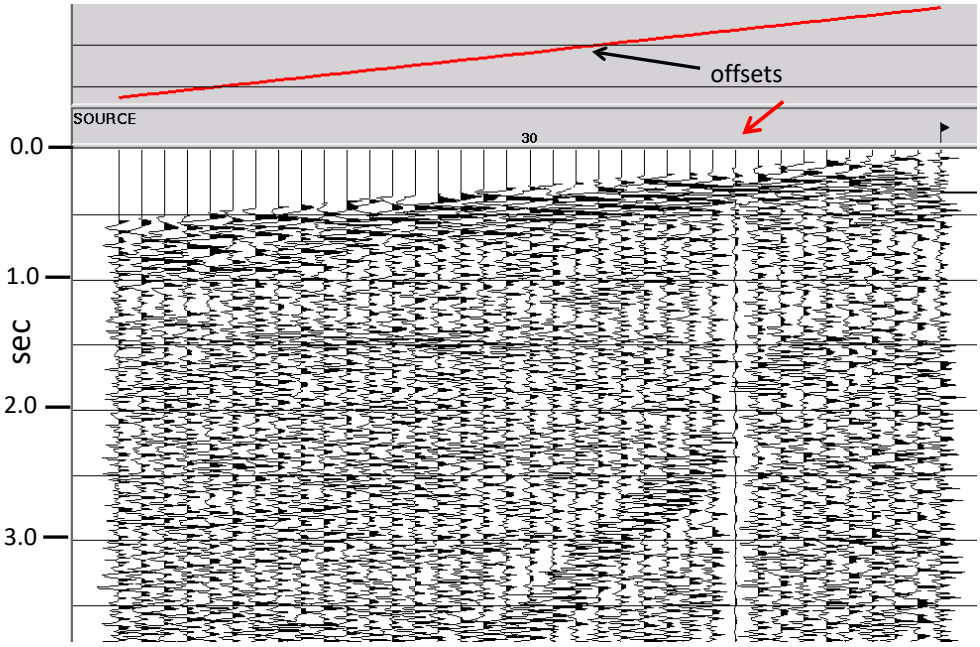

FIG. 38. Forward and inverse RT transform performed on ensemble in Figure 37. Leakage of neighboring trace amplitudes into dead trace is due to interpolation in the RT transform.

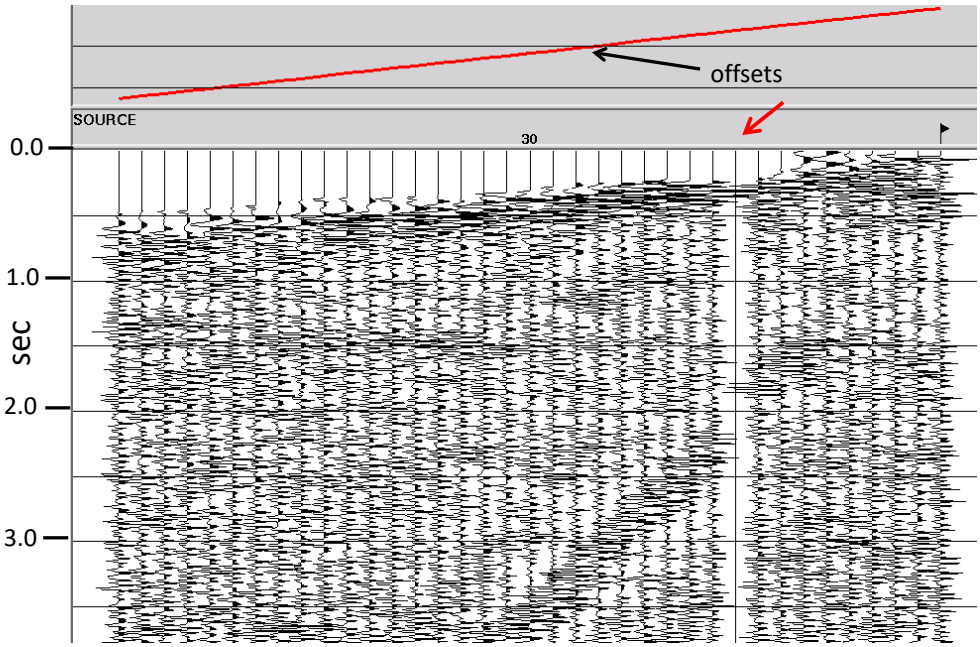

FIG. 39. Forward and inverse Tau-P transform performed on ensemble in Figure 37. No leakage into dead trace.

Figure 40 shows another common-azimuth bin ensemble from the Blackfoot PS data set, but with a decidedly nonlinear distribution of offsets, as can be seen in the trace header plot. There are also three dead traces visible in this ensemble. When this ensemble is subjected to the forward/inverse RT transform operation, the result is seen in Figure 41. The effect of the forced offset linearization in the inverse transform is quite obvious here,

with the 6 traces to the right of the source point flag in Figure 40 being expanded and interpolated over 30 traces in Figure 41, and the 56 traces to the left of the source point flag in Figure 40 being compressed into 32 in Figure 41. In this operation, the dead traces have been totally bridged by the interpolation, and much lateral detail in the compressed part of the ensemble has been lost. These two figures demonstrate why the RT transform in our current implementation is unsuitable for 3D raypath interferometry.

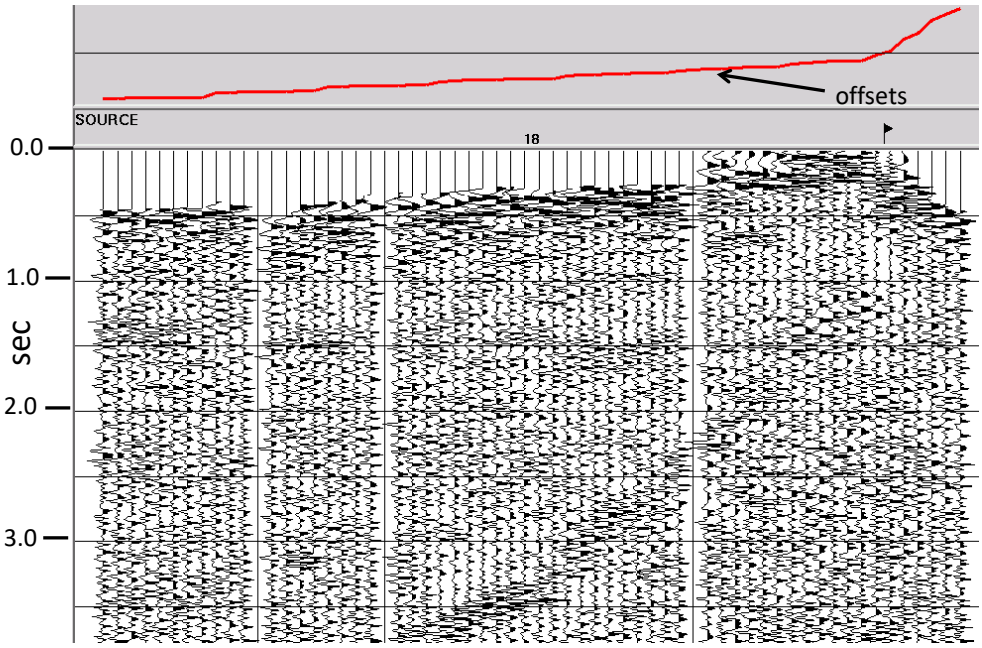

FIG. 40. Common-azimuth bin ensemble with nonlinear distribution of offset values.

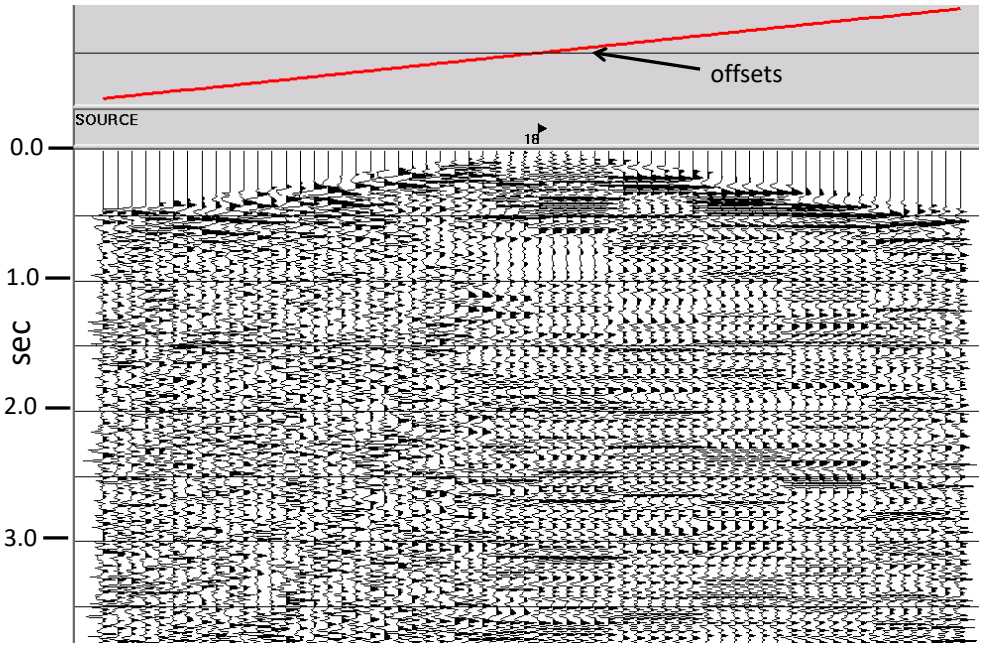

FIG. 41. Forward and inverse RT transform of ensemble in Figure 40. Traces to left of source location flag compressed, traces to the right of source flag interpolated.

Figure 42, in contrast, is the forward/inverse Tau-P transform of the common-azimuth ensemble in Figure 40, using a choice of aperture parameters which insure maximum fidelity. As can be seen in comparison with Figure 40, the data amplitudes are well-preserved in the forward/inverse operation, as is the trace header geometry. The storage requirements for the Tau-P transform with these aperture parameters, however, are quite prohibitive (this Tau-P transform requires 20 times the storage of the input ensemble). If we decrease the min/max slowness parameters which define the aperture by a factor of 2, the result of the forward/inverse Tau-P operation on the input common-azimuth ensemble is as shown in Figure 43. Compared with Figure 42, the lateral resolution is nearly as good, with a very slight hint of lateral smearing, and the storage requirements for the Tau-P transform are only half those for the transform used in Figure 42. Figures 44 and 45 show what happens when we try to reduce the aperture further, however (by a factor of 2.5 for Figure 44, and a factor of 5 for Figure 45). Clearly, lateral smearing quickly becomes unacceptable as the aperture is narrowed; it appears that preserving the fidelity of an ensemble similar to that in Figure 40 requires aperture parameters whose corresponding Tau-P transform then require storage approximately an order of magnitude greater than the input ensemble itself.

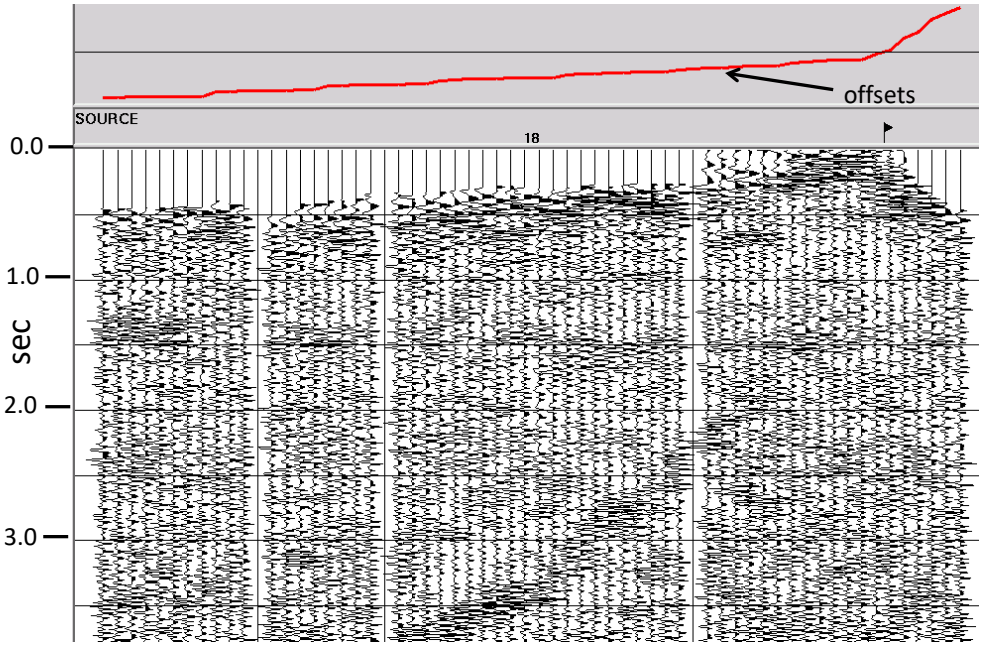

FIG. 42. Forward and inverse Tau-P transform of ensemble in Figure 40. All offsets preserved, all dead traces present, very little lateral smearing visible.

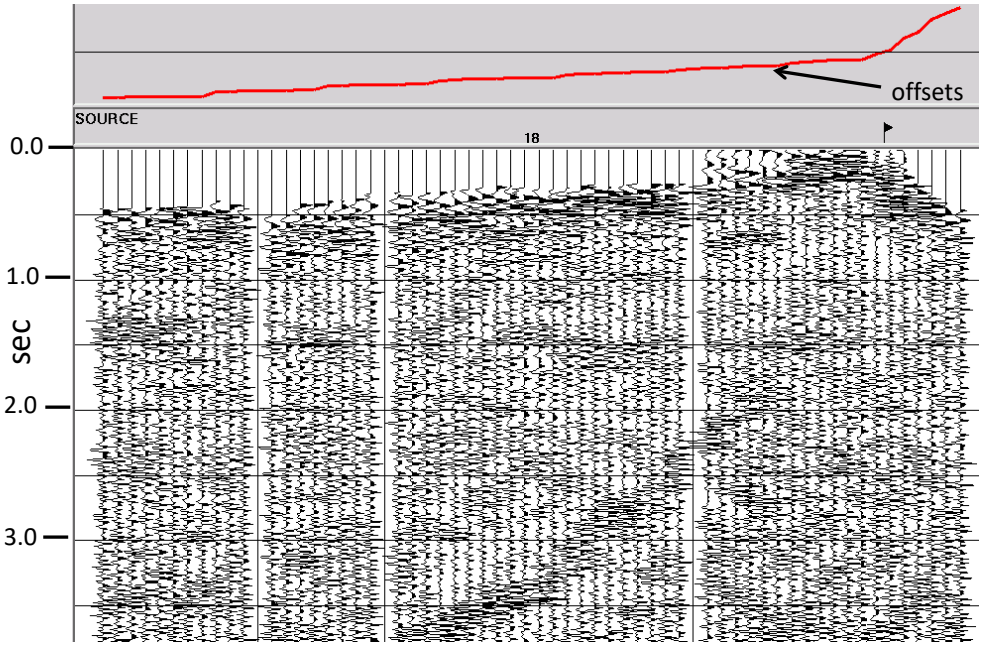

PS common-azimuth bin after forward/inverse Tau-P transform—
(-5000ms/km to 5000ms/km min/max slowness)

FIG. 43. Forward and inverse Tau-P transform of ensemble in Figure 40. Aperture restricted by a factor of 2.

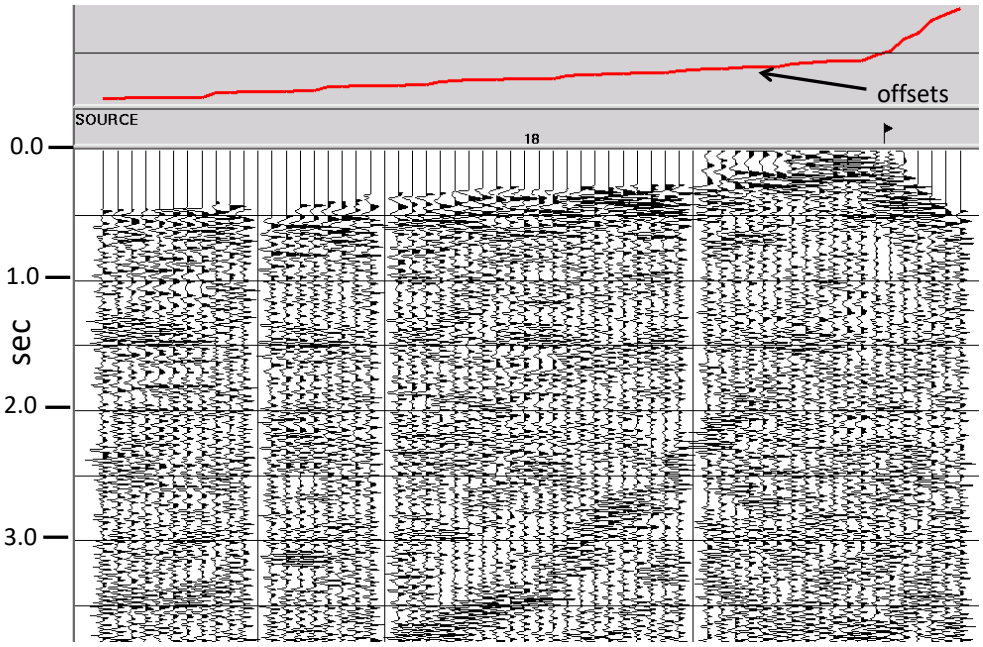

PS common-azimuth bin after forward/inverse Tau-P transform—
(-2000ms/km to 2000ms/km min/max slowness)

FIG. 44. Forward and inverse Tau-P transform of ensemble in Figure 40. Aperture restricted by a factor of 5. Some lateral smearing of events visible.

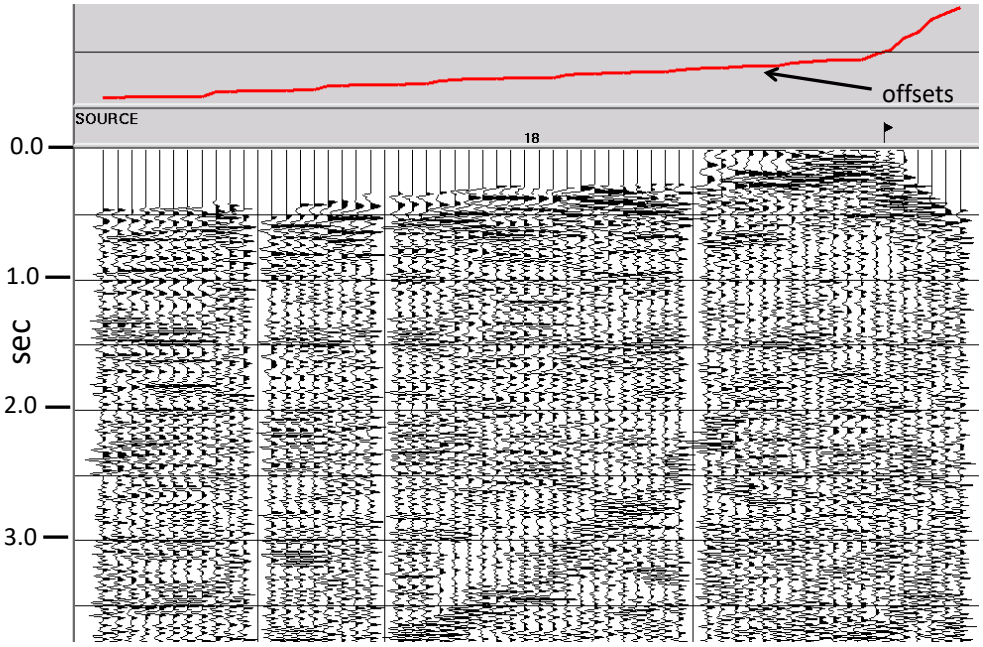

FIG. 45. Forward and inverse Tau-P transform of ensemble in Figure 40. Aperture restricted by a factor of 10. Lateral event smearing very prominent.

Figure 46 shows a third, and final common-azimuth ensemble with a nonlinear offset distribution. The offset distribution departs most significantly from linearity near the beginning and end of the ensemble, as seen in the 'sigmoidal' distribution shown in the trace header plot. The RT transform forward/inverse operation leads to the result shown in Figure 47, where the linearization of the offsets causes lateral stretching/interpolation of the amplitudes near the small/large offset ends of the ensemble, and lateral compression in the centre of the ensemble. The Tau-P transform forward/inverse result shown in Figure 48 is a much better result, but the limitations of the aperture can be seen in the lateral smearing of some traces in the ensemble (arrows). Figures 49 and 50, corresponding to more restrictive aperture choices (2.5 and 5 x reduction, as in Figures 44 and 45) are clearly too smeared to be acceptable for use in a procedure like raypath interferometry, which derives and applies near-surface corrections at distinct surface locations.

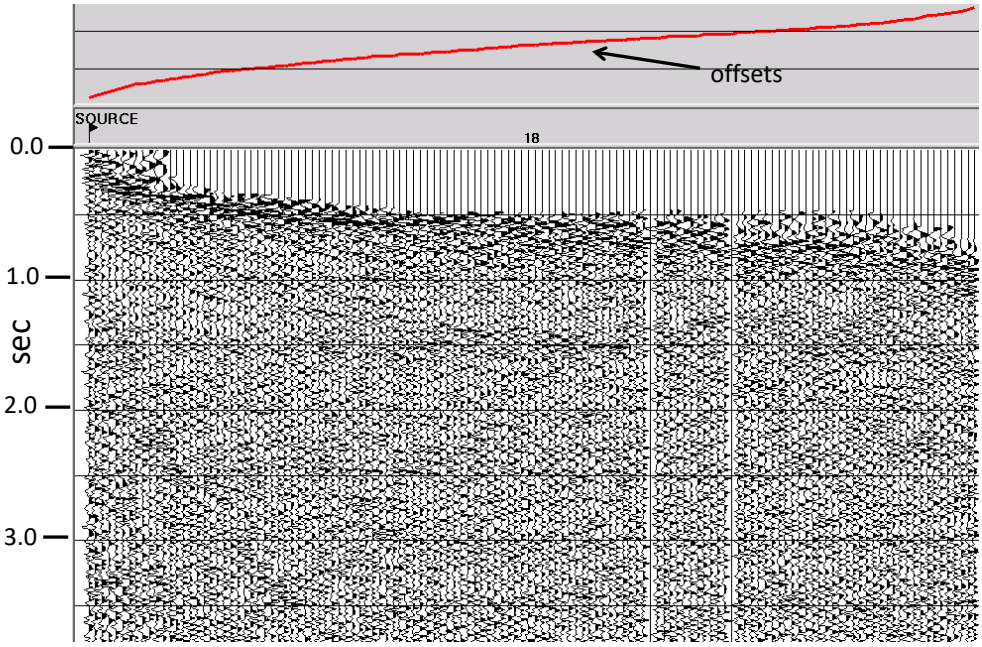

FIG. 46. Common-azimuth ensemble with 'sigmoidal' offset distribution.

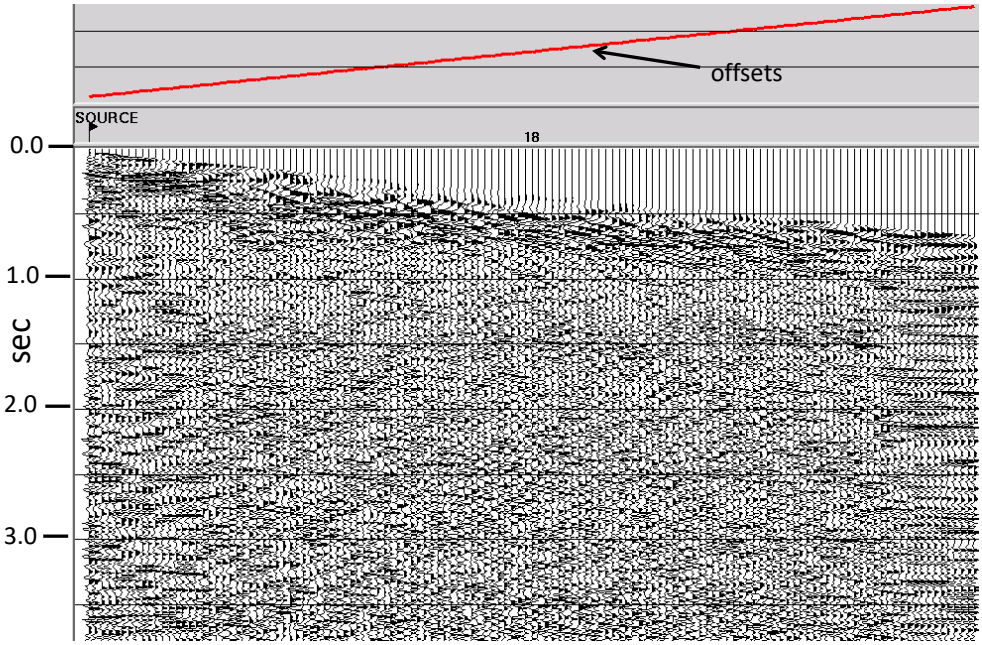

PS common-azimuth bin after forward and inverse RT. Since original offset distribution is relatively linear, distortion is not as pronounced.

FIG. 47. Forward and inverse RT transform of ensemble in Figure 46. Linearization of offsets in RT inverse leads to data smearing at both ends of this ensemble.

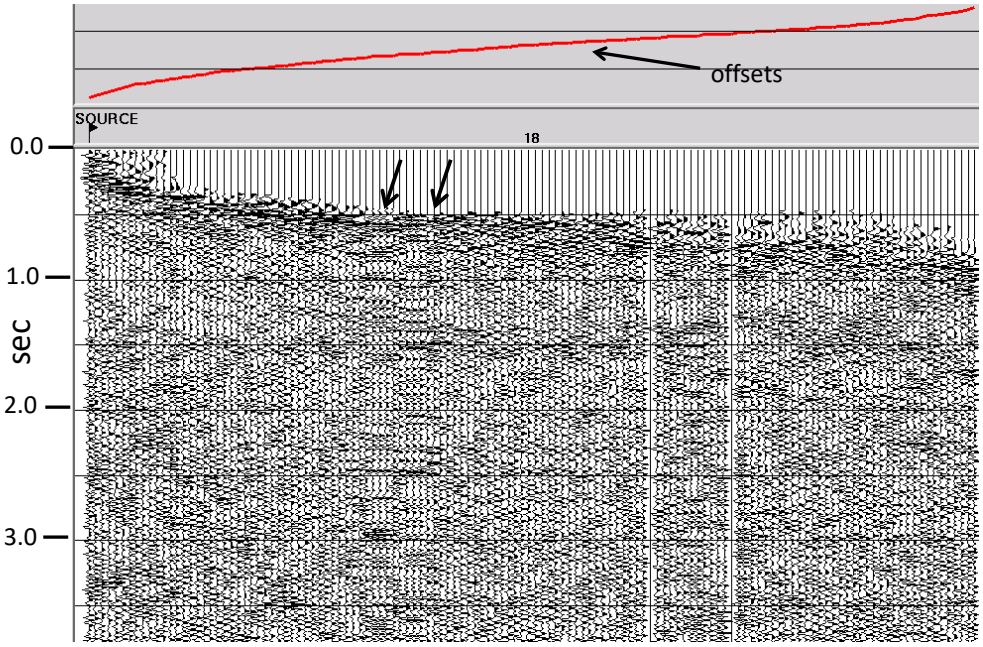

PS common-azimuth bin after forward/inverse Tau-P transform—
(-5000ms/km to 5000ms/km min/max slowness)

FIG. 48. Forward and inverse Tau-P transform of ensemble in Figure 46. Even with a wide aperture, data sometimes smears in Tau-P (arrows).

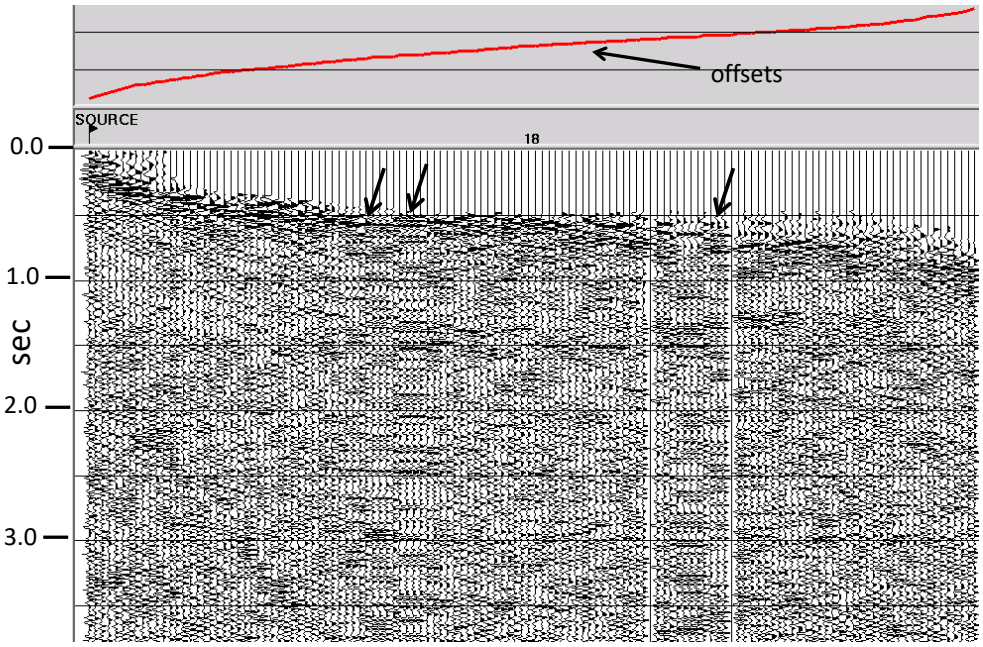

PS common-azimuth bin after forward/inverse Tau-P transform—
(-2000ms/km to 2000ms/km min/max slowness)

FIG. 49. Forward and inverse Tau-P transform of ensemble in Figure 46, with aperture restricted by a factor of 2.5 from Figure 48. Event smearing becomes more noticeable.

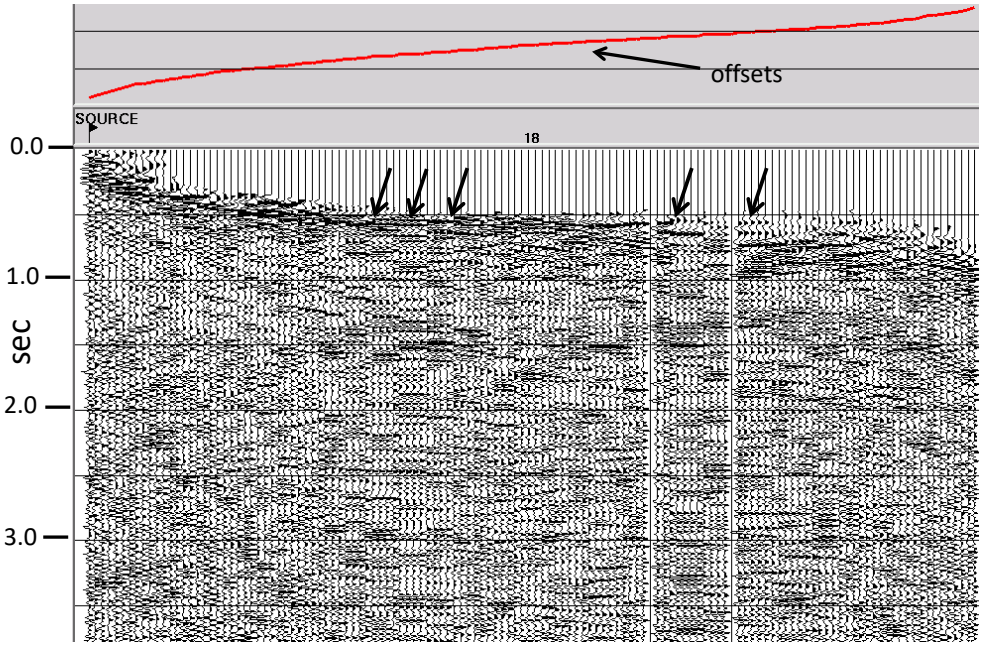

FIG. 50. Forward and inverse Tau-P transform of ensemble in Figure 46. Aperture restriction of a factor of 5 leads to even more event smearing.

CONCLUSIONS

We have shown that the technique known as raypath interferometry can be extended from 2D to 3D. While we haven't yet applied the complete raypath interferometry procedure in 3D, we have outlined one approach for extending the method to 3D, and we have identified the particular difficulties encountered with this approach, specifically the choice of transform used to move the 3D data set from Cartesian coordinates to a 3D raypath domain and back to Cartesian coordinates. We have also shown some comparisons of trace ensembles from the Blackfoot 3D 3C data set (both vertical component and radial component) which strongly suggest the ultimate success of our approach, once transform difficulties are overcome.

Specifically:

- The raypath interferometry concept of the surface function can be easily expanded from 2D to 3D by simply adding azimuth as a third independent variable, in addition to surface location (station number) and raypath parameter.

- To accommodate the 3D surface function, a new trace header, source-receiver azimuth, can be added to seismic traces in a 3D data set, and used to create common-azimuth bins.

- When common-azimuth bins form the basis for gathering trace ensembles from 3D data sets, a 2D transform can be used to move the seismic data from the

offset-time domain to a raypath domain and back. This is an approximation, however, which improves with the fold of the survey.

- When choosing dimensions for common-azimuth bins, there is a trade-off between the angular width of the bins and the trace population and distribution in the bins, wider bins having larger and more regularly distributed trace populations.

- The reference wavefield must be smoothed in two dimensions (not necessarily orthogonal) in order to extract full 3D surface information.

- Our current RT transform is designed to handle only trace ensembles with linearly distributed source-receiver offsets, so it cannot be used for a full-scale application of 3D raypath interferometry. We can, however, test interferometry results for trace ensembles from a 3D survey whose actual offset distribution is `somewhat` linear.

- The Tau-P transform appears to be the most appropriate 2D raypath transform for applying 3D raypath interferometry, but it displays some lateral trace smearing and requires a large amount of storage to preserve adequate data fidelity.

ACKNOWLEDGEMENTS

The author gratefully acknowledges funding from CREWES sponsors and NSERC (Natural Science and Engineering Research Council of Canada) through the grant CRDPJ 461179-13., and thanks various colleagues for stimulating discussions.

REFERENCES

Bakulin, A. and Calvert, R., 2006, The virtual source method: theory and case study, Geophysics, **71**, S1139-S1150.

Claerbout, J.F., 1975, Slant-stacks and radial traces: Stanford Expl. Project Report, **SEP-5**, 1-12.

Claerbout, J.F., 1983, Ground Roll and Radial Traces, Stanford Exploration Project Report, **SEP-35**, pp 43-53.

Cova, R., Henley, D.C., and Innanen, K.A.H., 2013a, Non-stationary shear wave statics in the radial trace domain, CREWES Research Report, **25**.

Cova, R., Henley, D.C., and Innanen, K.A.H., 2013b, An interferometric solution for raypath-consistent shear wave statics, CREWES Research Report, **25**.

Cova, R., Henley, D.C., and Innanen, K.A.H., 2014a, Inverting raypath dependent delay times to compute S-wave velocities in the near surface, CREWES Research Report, **26**.

Cova, R., Henley, D.C., and Innanen, K.A.H., 2014b, Making shear wave statics actual statics using radial trace and tau-p transforms, CREWES Research Report, **26**.

Cova, R., Wei, X., and Innanen, K.A.H., 2015, Shear wave near-surface corrections in the tau-p domain: a case study, CREWES Research Report, **27**.

Henley, D.C., 1999, Radial trace computational algorithms at CREWES, CREWES Research Report **11**.

Henley, D.C., 1999, Demonstration of radial trace domain filtering on the Shaganappi 1998 geotechnical survey, CREWES Research Report **11**.

Henley, D.C., 2006, Application of raypath-dependent statics to Arctic seismic data: CREWES Research Report, **18**.

Henley, D.C., and Daley, P.F., 2007, Connecting statics deconvolution and seismic interferometry, CREWES Research Report **19**.

Henley, D.C., 2012a, Interferometric application of static corrections, Geophysics, **77**, No. 1, pp Q1-Q13.

Henley, D.C., 2012b, Interference and the art of static correction: raypath interferometry at Hussar, CREWES Research Report **24**.

Henley, D.C. 2014, Through a glass darkly: improving raypath interferometry, CREWES Research Report **26.**

Henley, D.C., 2015, 3D or not 3D, that is the question: raypath interferometry in 3D processing, CREWES Research Report **27**.

Lawton, D.C., 1996, Design review of Blackfoot 3C-3D seismic survey, CREWES Research Report **8**.

Ottolini, R., 1981, Downward Continuation of Common Midpoint Gathers by Transformation into Snell Trace Coordinates, Stanford Exploration Project Report, **SEP-26**, pp 83-94.